

Recirculating Quantum Photonic Networks for Fast Deterministic Quantum Information Processing

Emil Grovn,^{1, 2, *} Matias Bundgaard-Nielsen,^{1, 2} Jesper Mørk,^{1, 2} Dirk Englund,³ and Mikkel Heuck^{1, 2, †}

¹*DTU Electro, Technical University of Denmark, Building 343, 2800 Kgs. Lyngby, Denmark*

²*NanoPhoton - Center for Nanophotonics, Technical University of Denmark, Building 343, 2800 Kgs. Lyngby, Denmark*

³*Department of Electrical Engineering and Computer Science, Massachusetts Institute of Technology, 77 Massachusetts Avenue, Cambridge, Massachusetts 02139, USA*

(Dated: February 12, 2026)

A fundamental challenge in photonics-based deterministic quantum information processing is to realize key transformations on time scales shorter than those of detrimental decoherence and loss mechanisms. This challenge has been addressed through device-focused approaches that aim to increase nonlinear interactions relative to decoherence rates. In this work, we adopt a complementary architecture-focused approach by proposing a recirculating quantum photonic network (RQPN) that minimizes the duration of quantum information processing tasks, thereby reducing the requirements on nonlinear interaction rates. The RQPN consists of a network of all-to-all connected nonlinear cavities with dynamically controlled waveguide couplings, and it processes information by capturing a photonic input state, recirculating photons between the cavities, and releasing a photonic output state. We demonstrate the RQPN's architectural advantage through two examples: first, we show that processing all qubits simultaneously yields faster operations than single- and two-qubit decompositions of the three-qubit Toffoli gate. Second, we demonstrate implementations of a measurement-free correction for single-photon loss, achieving up to seven-fold speedups and significantly improved hardware efficiency relative to state-of-the-art architecture proposals. Our work shows that a single hardware-efficient recirculating architecture substantially reduces the temporal overhead of multi-qubit gates and quantum error correction, thereby lowering the barrier to experimental realizations of deterministic photonic quantum information processing.

I. INTRODUCTION

Photons can travel over long distances with low loss and decoherence in optical fibers, making photonic qubits an excellent candidate for, e.g., secure communication and distributed quantum computing [1]. To perform universal qubit operations, both single- and two-qubit gates are needed [2]. With dual-rail encoding, single-qubit gates are easily realized using linear optical elements [3], while two-qubit entangling gates require nonlinear transformations of photonic modes. Measurement-induced effective nonlinearities are being pursued for universal quantum computing [3–5]. However, the resulting probabilistic gates require multiplexing, leading to a significant resource overhead.

Deterministic entangling gates based on matter-mediated optical nonlinearities are challenged by fundamental limitations related to wave packet distortions [6–9] and small nonlinear interaction rates in materials used for photonic integrated circuits [3, 10]. These theoretical challenges have been addressed through device-focused approaches to implementing high-fidelity controlled-sign (*CZ*) gates [11–19]. Additionally, impressive experimental demonstrations have improved the strength of nonlinear interaction rates for atom-like systems relative to loss and decoherence rates [20–23], although not yet to levels that enable high-fidelity *CZ* gates [19].

The challenges of deterministic two-qubit logic exacerbate the difficulties of realizing complex quantum information processing (QIP) tasks that require circuits with many gates. This motivates complementary architecture-focused approaches to implement complex QIP tasks directly rather than decomposing them into circuits with single- and two-qubit gates.

In this work, we adopt this approach by proposing a recirculating quantum photonic network (RQPN) architecture that reduces the duration of complex QIP tasks through dynamic control of multi-photon interactions. By considering the implementation of a three-qubit Toffoli gate in dual-rail encoding, we find a reduced gate duration by processing all qubits simultaneously rather than using decompositions into single- and two-qubit (or -qutrit) gates. In another example, we find implementations of a one-way quantum repeater capable of correcting single-photon loss. This example demonstrates that the RQPN provides significant improvements in time and hardware efficiency relative to state-of-the-art architectures based on hardware-tailored gates [24] or neural networks [25–27].

The RQPN, illustrated in Fig. 1(a), consists of dynamic nonlinear cavities connected to a linear mixing circuit composed of Mach-Zehnder interferometers. The nonlinear cavities have controllable resonance frequencies, $\omega_m^c(t)$, and waveguide couplings, $\kappa_m(t)$. This dynamic control enables input (output) quantum states to be captured (released) by the nonlinear cavities, as shown in Fig. 1(b). After photon capture, the RQPN

* Contact author: e.grovn@gmail.com

† Contact author: mheu@dtu.dk

is in its recirculating configuration, where the dynamic control is used to steer the quantum state toward a targeted output by recirculating photons between the nonlinear cavities via the mixing circuit, as illustrated in Figs. 1(a,c). Experimental demonstrations of such controllable cavities are found, e.g., in Refs. [28–31], and details on their use for implementing deterministic *CZ* gates in Refs. [17–19]. Here, we focus on optimizing the controls, $\omega_m(t)$ and $\kappa_m(t)$, to minimize the duration of QIP tasks with the RQPN in its recirculating configuration. In practical implementations, we envision the nonlinear cavities being connected to the input/output channels and mixing circuit via fast routers [32] to switch between the capture/release and recirculating configurations.

This manuscript is organized as follows: Section II presents the RQPN model and numerical framework used to optimize the controls. In Sec. III, we consider implementations of the three-qubit Toffoli gate based on self-phase modulation (SPM). Section IV presents our results on measurement-free implementations of a one-way repeater using a bosonic encoding [33, 34] with nonlinearities originating from SPM or interactions with two-level emitters (TLEs). Section V contains a discussion of the path toward experimental realizations of RQPNs. Finally, we conclude and provide an outlook for future work in Section VI.

II. MODEL AND OPTIMAL CONTROL

We assume a perfect fidelity of the capture (release) of the input (output) quantum state of the RQPN before (after) the evolution in the recirculating configuration. This assumption is valid for sufficiently short input (output) pulses compared to the characteristic time scale of the nonlinear interactions, $1/\Gamma_{\text{NL}}$ [17–19]. In the following, we thus neglect the duration of the capture and release processes and solely focus on describing and optimizing the dynamics of the RQPN in its recirculating configuration. To describe the RQPN in Fig. 1, we use the SLH framework [35–37] to only consider the degrees of freedom in the localized quantum systems (cavities). In the SLH framework, the influence on the cavity field from the continuum field of the waveguide is described as interactions with a broadband bosonic bath [37–39]. We assume the carrier frequencies of the waveguide fields are centered around ω_0 , and the cavity-waveguide interactions occur within a frequency window, Ω_{int} , around ω_0 . Then, the assumptions of the SLH framework require that the cavity-waveguide coupling is approximately frequency-independent across the spectral range of coupling, so the interaction can be described by a Markovian coupling rate $\kappa_m(t)$. Furthermore, Ω_{int} must be large compared to the characteristic rates of the localized system: $\kappa_m(t)$, $\delta_m(t) = \omega_m(t) - \omega_0$, and Γ_{NL} , as well as the modulation bandwidth of the controls Ω_{mod} . Fi-

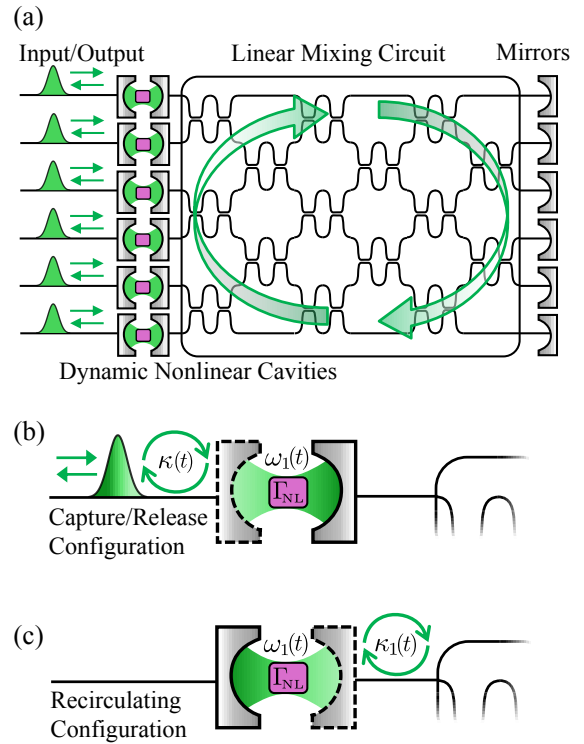


FIG. 1. (a) Sketch of the RQPN architecture. Dynamic nonlinear cavities are coupled to a linear mixing circuit composed of Mach-Zehnder interferometers, and the network is closed by mirrors on the right. The waveguide coupling of the nonlinear cavities is controllable. (b) To capture and release photonic quantum states from the cavities, they may be opened towards the input/output channel with a controllable coupling, $\kappa(t)$ (dashed outline of the mirror). (c) When a quantum state is trapped in the cavities, the RQPN is in its recirculating configuration, with the cavities closed towards the input/output channels (solid outline of the mirrors). In this configuration, photons interact in the cavities with a nonlinear interaction rate, Γ_{NL} , and the controllable resonances, $\omega_m(t)$, and waveguide couplings, $\kappa_m(t)$, are optimized to implement a targeted QIP task. Note that (b) and (c) illustrate the top cavity ($m = 1$). Practically, we envision the nonlinear cavities having only one mirror with a controllable coupling, and the configurations in (b) and (c) to be realized using fast routers [32].

nally, the propagation time of the waveguide fields across the mixing circuit, T_{prop} , is assumed to be infinitesimal in the SLH framework, so the corresponding bandwidth must be much larger than all the characteristic rates of the localized systems: $1/T_{\text{prop}} \gg \kappa_m(t), \delta_m(t), \Gamma_{\text{NL}}$, and Ω_{mod} . For RQPNs with sufficiently large mixing circuits or cavities with fast dynamics or modulation, the effect of finite propagation times must be taken into account. This involves descriptions that include the Hilbert space of propagating fields. Computationally tractable approaches to this problem could include matrix product states or explicit methods [40]. Addressing this challenge is left for future work.

A. Recirculating Circuit Model

In its recirculating configuration, the RQPN is described by the Hamiltonian (Supplemental Material SI [41])

$$\hat{H}(t) = \hbar \sum_m \delta_m^c(t) \hat{a}_m^\dagger \hat{a}_m + \hbar \sum_n \sum_m C_{nm} \sqrt{\kappa_n^*(t) \kappa_m(t)} \hat{a}_n^\dagger \hat{a}_m + \hat{H}_{\text{NL}}. \quad (1)$$

In each sum, the index runs from 1 to M , where M is the number of cavities. Each cavity, m , is considered to have a single mode with annihilation operator \hat{a}_m and creation operator \hat{a}_m^\dagger . The corresponding n -photon state is denoted $|n_m\rangle$. We use a rotating frame oscillating at ω_0 such that $\delta_m^c(t) = \omega_m^c(t) - \omega_0$, where $\omega_m^c(t)$ is the controllable resonance of each cavity. We added the superscript c to distinguish cavity resonances from TLE transition frequencies introduced below. The linear mixing circuit couples all the cavities with controllable rates, $C_{nm} \sqrt{\kappa_n^*(t) \kappa_m(t)}$, where $\kappa_m(t)$ is the cavity-waveguide coupling of cavity m , assumed to be real and positive. The coupling matrix, \mathbf{C} , is related to the scattering matrix, \mathbf{S} , that defines the unitary transformation of modes when going from left to right through the mixing circuit and can be constructed with a mesh of Mach-Zehnder interferometers [42, 43]. The relation between \mathbf{C} and \mathbf{S} is

$$\mathbf{C} = \text{Im} \left\{ \mathbf{S} \mathbf{S}^T (\mathbf{I} - \mathbf{S} \mathbf{S}^T)^{-1} \right\}, \quad (2)$$

where Im denotes the (elementwise) imaginary part and \mathbf{I} is the identity matrix. Since \mathbf{S} can be any unitary matrix, we prove in Supplemental Material SII [41] that \mathbf{C} can be any real symmetric matrix. The nonlinear Hamiltonian, \hat{H}_{NL} , describes the optically nonlinear internal dynamics of the cavities. We consider, separately, the two cases of SPM

$$\hat{H}_{\text{SPM}} = -\hbar \chi_3 \sum_m \hat{a}_m^\dagger \hat{a}_m^\dagger \hat{a}_m \hat{a}_m, \quad (3)$$

and interactions with TLEs

$$\hat{H}_{\text{JC}} = \hbar g \sum_m (\hat{\sigma}_m \hat{a}_m^\dagger + \hat{\sigma}_m^\dagger \hat{a}_m). \quad (4)$$

The nonlinear interaction rate, Γ_{NL} , is χ_3 for SPM interactions and g for the Jaynes-Cummings Hamiltonian [44]. For interactions with TLEs, we also consider the emitter transition energy to be controllable, as described by the Hamiltonian

$$\hat{H}_{\text{TLE}} = \sum_m \hbar \delta_m^e(t) \hat{\sigma}_m^\dagger \hat{\sigma}_m, \quad (5)$$

where $\delta_m^e(t) = \omega_m^e(t) - \omega_0$, $\hat{\sigma}_m = |g_m\rangle\langle e_m|$, and $\hat{\sigma}_m^\dagger = |e_m\rangle\langle g_m|$, with $|g_m\rangle$ and $|e_m\rangle$ being the ground and excited state of the TLE in cavity m and $\omega_m^e(t)$ being the controllable transition frequency.

B. Numerical Control Framework

In the RQPN simulation, we neglect loss and decoherence effects from the surrounding environment. We optimize the controls to minimize the quantum process duration, T , which, for entangling processes, is ultimately limited by the nonlinear coupling rate, Γ_{NL} . To enable comparisons of time efficiency between different material platforms and architectures, we define a dimensionless process duration, T_η , by measuring the duration in units of the inverse nonlinear interaction rate, $T = T_\eta / \Gamma_{\text{NL}}$. Minimizing T_η lowers the requirement on the size of the nonlinear rate relative to the dominant decoherence rate, thereby lowering the barrier for experimental demonstrations of quantum information processing.

We specify a QIP task by a transformation of a set of input states to a targeted set of output states

$$|\psi^{(n)}(T)\rangle = \hat{U}_{\text{tar}} |\psi_{\text{in}}^{(n)}\rangle, \quad n = 1, \dots, N_{\text{task}}. \quad (6)$$

The controls are time-signals parametrized as piecewise-constant functions over N_{bin} time bins [45–47]. Thus, the mapping from the initial to the final state is

$$|\psi(T)\rangle = (\hat{U}_{N_{\text{bin}}} \dots \hat{U}_2 \hat{U}_1) |\psi_{\text{in}}\rangle = \hat{U}_{\text{RQPN}} |\psi_{\text{in}}\rangle, \quad (7)$$

where

$$\hat{U}_p = \exp\left(-i \hat{H}_p \Delta t_p / \hbar\right), \quad (8)$$

and \hat{H}_p is the Hamiltonian of the p 'th time bin. We optimize the coupling rates $\kappa_m(t_p)$, detunings $\delta_m^c(t_p)$ and $\delta_m^e(t_p)$ (t_p being the time in the p 'th bin), time bin durations Δt_p , and the coupling matrix \mathbf{C} (see Supplemental Material SIII [41] for parameterization details).

The time evolution in Eqs. (7) and (8) is evaluated numerically in Python using the open-source framework **Dynamiqs** [48], which utilizes **Jax** for the automatic differentiation back-end [49]. We use the gradient-descent-based algorithm **Adam** [50] to minimize a cost function, $\mathcal{E}(\boldsymbol{\theta})$, which depends on the vector $\boldsymbol{\theta}$ containing all the trainable parameters (see Supplemental Material SIII [41] for details of the optimization procedure). The primary optimization objective is to maximize the overlap between the output and target states for all N_{task} inputs specified by the QIP task under consideration. Therefore, the cost function contains a term $\mathcal{E}_{\mathcal{I}} = \ln(\mathcal{I})$, with the infidelity \mathcal{I} defined by

$$\mathcal{I} = 1 - \left| \frac{1}{N_{\text{task}}} \sum_{n=1}^{N_{\text{task}}} \langle \psi_{\text{in}}^{(n)} | \hat{U}_{\text{tar}}^\dagger \hat{U}_{\text{RQPN}} | \psi_{\text{in}}^{(n)} \rangle \right|^2. \quad (9)$$

We stop the optimization once \mathcal{I} drops below a threshold, \mathcal{I}_{th} , typically set to $\mathcal{I}_{\text{th}} = 0.1\%$. Additional terms may be added to \mathcal{E} to penalize large control bandwidths, while the control amplitudes are explicitly bounded by our choice of parameterization, as described in Supplemental Material SIII [41]. The time steps Δt_p , and

thereby the duration $T = \sum_{p=1}^{N_{\text{bin}}} \Delta t_p$, are also explicitly bounded from below and above. To minimize the process duration, we consider many different optimization configurations and gradually reduce the upper bound for each configuration until $\mathcal{I} \leq \mathcal{I}_{\text{th}}$ cannot be achieved.

III. ADVANTAGE OF MULTI-QUBIT PROCESSING

The coupling matrix, \mathbf{C} , can be chosen so that the RQPN exhibits all-to-all coupling between the nonlinear cavities throughout the time evolution of the recirculating configuration. Therefore, for a given QIP task, we can search for a direct implementation of the full transformation rather than decomposing it into smaller transformations, each involving fewer photons and modes. To illustrate the advantage of this all-to-all connectivity and multi-qubit processing, we consider the three-qubit Toffoli gate on dual-rail encoded qubits, implemented using the SPM interactions described by the Hamiltonian in Eq. (3). We compare a direct implementation to decompositions into single- and two-qubit (or qutrit) gates.

A. Decomposition of the Toffoli Gate using Single- and Two-Qubit Gates

Single-qubit gates along with the two-qubit CZ gate provide a universal gate set, which means that any N -qubit unitary operation can be decomposed using these gates [2]. In dual-rail encoding, any single-qubit gate can be realized by linear transformations of optical modes and is thus controlled by the cavity-cavity coupling term and cavity detuning term in Eq. (1). Their duration, i.e., the time required to transform the input state into the desired output state, is limited only by the amplitude and bandwidth of $\kappa_m(t)$ and $\delta_m^c(t)$, and is negligible in practice where the SPM strength, χ_3 , is the limiting physical property of the system. On the other hand, two-qubit entangling gates, such as the CZ gate, require nonlinear transformations of optical modes [3], so their duration is limited by χ_3 . In Supplemental Material SIV A [41], we prove that, when using SPM nonlinearities, the CZ -gate duration is bounded from below by $(\pi/4)/\chi_3$ for an infidelity of $\mathcal{I} = 0$ and by $0.754/\chi_3$ for $\mathcal{I} = 0.1\%$. We find both an analytical implementation with this duration and a numerical RQPN implementation with a duration of $0.773/\chi_3$ for $\mathcal{I} = 0.1\%$. The minimum number of CZ gates required to implement the three-qubit Toffoli gate is six [51]. However, if an additional optical mode is available, one of the qubits may be represented as a qutrit with three logical states $\{|0\rangle_L, |1\rangle_L, |2\rangle_L\}$. A CZ gate operating on a qubit and a qutrit, defined by an

operator \hat{U}_{CZ} , causes the following transformations [51]

$$\begin{aligned} \hat{U}_{CZ} |0, 0\rangle_L &= |0, 0\rangle_L, & \hat{U}_{CZ} |0, 1\rangle_L &= |0, 1\rangle_L, \\ \hat{U}_{CZ} |1, 0\rangle_L &= |1, 0\rangle_L, & \hat{U}_{CZ} |1, 1\rangle_L &= -|1, 1\rangle_L, \\ \hat{U}_{CZ} |0, 2\rangle_L &= |0, 2\rangle_L, & \hat{U}_{CZ} |1, 2\rangle_L &= |1, 2\rangle_L. \end{aligned} \quad (10)$$

With access to an additional mode and the qubit-qutrit CZ operator \hat{U}_{CZ} , a decomposition of the Toffoli gate only requires three qubit-qutrit CZ gates [51]. In Supplemental Material IV B [41], we prove that the duration of \hat{U}_{CZ} is bounded from below by $(\pi/4)/\chi_3$ for $\mathcal{I} = 0$ and $0.754/\chi_3$ for $\mathcal{I} = 0.1\%$, but the existence of an implementation with this duration is not guaranteed. Numerically, we find an RQPN implementation of the qubit-qutrit CZ gate with a duration of $0.89/\chi_3$ for $\mathcal{I} = 0.1\%$, which, to the best of our knowledge, is the fastest existing implementation with SPM interactions. The corresponding Toffoli gate duration is $2.67/\chi_3$. Operating on two photons in five modes rather than four modes provides a significant speedup of the three-qubit Toffoli gate, in practice, from $4.64/\chi_3$ (with $\mathcal{I} = 0.86\%$ for the full Toffoli gate) to $2.67/\chi_3$ (with $\mathcal{I} = 0.30\%$ for the full Toffoli gate) using qubit-qubit and qubit-qutrit CZ gates with infidelity $\mathcal{I} = 0.1\%$, respectively. In the next section, we investigate the potential speedup when operating on all three photons in all six modes simultaneously using the RQPN architecture.

B. Direct Implementation of the Toffoli Gate

The RQPN used to implement the Toffoli gate is illustrated in Fig. 2(a). We optimize the controls in the recirculating configuration with $N_{\text{bin}} = 80$ to implement the Toffoli gate. Figure 2(b) shows the control fields for cavity $m = 6$, as an example, from an optimization resulting in $\mathcal{I} < 0.30\%$ - see Supplemental Material SV [41] for the controls of the remaining cavities, the optimized coupling matrix, and the state evolution for the eight computational basis states. The duration of the Toffoli gate is reduced to $T = 2.00/\chi_3$ when using the RQPN to simultaneously process all three qubits using all six modes, beating the implementations with qubit-qubit CZ gates and qubit-qutrit CZ gates by a factor of 2.32 and 1.34, respectively. We ran the optimization using a fixed duration of $T = 2.00/\chi_3$ and without constraining the control amplitudes and bandwidths to beat the analytical lower bound of $2.32/\chi_3$ with qubit-qutrit CZ gates. This demonstrates the fundamental advantage in time efficiency of processing all photons in all modes simultaneously. Our optimization procedure does not exhaust the space of possible implementations, so it is possible that a faster RQPN implementation exists.

For SPM interactions, n -photon states acquire a nonlinear phase with a rate $n(n-1)\chi_3$. Therefore, the maximum rate of the fully connected RQPN ($6\chi_3$) is three times larger than that of the decompositions ($2\chi_3$). Figure 2(c) shows the probability of three photons all occu-

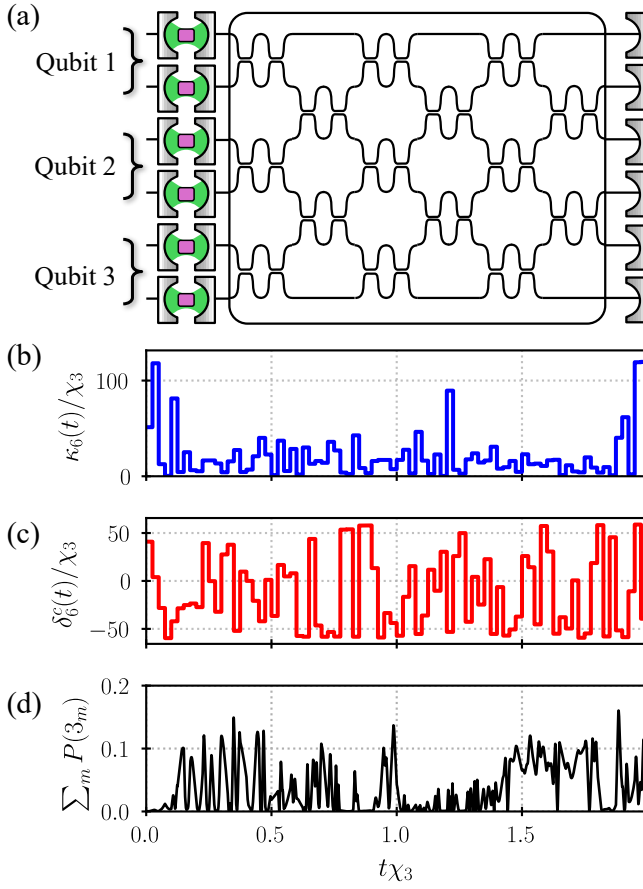


FIG. 2. Direct implementation of the three-qubit Toffoli gate with dual-rail encoding. (a) RQPN architecture with SPM nonlinearities and six cavities to encode three qubits. (b) Optimized cavity-waveguide coupling and (c) detuning for cavity $m = 6$. (d) Probability of three photons occupying the same cavity, for the initial state $|\psi_{\text{in}}\rangle = |0,0,0\rangle_L$. The probability of n photons occupying cavity m is $P(n_m) = |\langle\psi(t)|n_m\rangle|^2$. The result was achieved using $N_{\text{bin}} = 80$, a fixed duration $T = 2.0/\chi_3$, and trainable cavity-waveguide coupling, detuning, and coupling matrix \mathbf{C} . Additional information for the optimization and result is in Supplemental Material SV [41], Fig. 6.

pying the same cavity for the logical input $|0,0,0\rangle_L$. We observe that the optimizer makes significant use of the stronger nonlinearity.

IV. MEASUREMENT-FREE CORRECTION OF SINGLE-PHOTON LOSS

A key requirement for utility-scale quantum computing is the ability to correct errors [52–54]. Photon loss is the dominant error channel of most photonics-based systems [10] and a major obstacle for scalable photonic quantum computing architectures [5, 55]. Photon-loss correction is also crucial in quantum communication [56]. In the following, we correct for single-photon loss using the

RQPN. We consider the following multi-photon bosonic encoding [33]:

$$|0\rangle_L = \frac{1}{\sqrt{2}} (|4_1, 0_2\rangle + |0_1, 4_2\rangle), \quad |1\rangle_L = |2_1, 2_2\rangle, \quad (11)$$

where each logical state contains four photons distributed across two modes. Miatio *et al.* [57] proposed a theoretical scheme that uses the encoding in Eq. (11) for measurement-free correction of single-photon loss, also denoted a measurement-free one-way quantum repeater. We are aware of only two proposals for implementations of this task: the first uses a neural network architecture [25] with SPM interactions, and the second uses a circuit of triply-resonant cavities with interactions based on second-harmonic generation [24]. In the following, we consider RQPN implementations and compare their time and hardware efficiency with these alternative architectures.

A. Definition of the One-Way Repeater Task

In measurement-free correction of single-photon loss, we consider a code state $|C\rangle = \alpha|0\rangle_L + \beta|1\rangle_L$ traveling through a lossy quantum channel. After propagation, the correctable error states are $|E1\rangle = \alpha|3_1, 0_2\rangle + \beta|1_1, 2_2\rangle$ and $|E2\rangle = \alpha|0_1, 3_2\rangle + \beta|2_1, 1_2\rangle$, where a photon was lost from mode 1 or 2, respectively. For a channel with, e.g., a 10% risk of losing a single photon in either mode, there is a 1% chance of uncorrectable multi-photon loss [24]. A unitary transformation maps orthogonal inputs to orthogonal outputs, so a measurement-free operation that maps any input $|\psi_{\text{in}}\rangle = \{|C\rangle, |E1\rangle, |E2\rangle\}$ to the same output $|C\rangle$ requires an ancillary quantum system. The targeted transformation of the repeater is

$$\begin{aligned} \text{No loss : } & |C\rangle \otimes |A0\rangle \rightarrow |C\rangle \otimes |A0\rangle \\ \text{Mode 1 loss : } & |E1\rangle \otimes |A0\rangle \rightarrow |C\rangle \otimes |A1\rangle \\ \text{Mode 2 loss : } & |E2\rangle \otimes |A0\rangle \rightarrow |C\rangle \otimes |A2\rangle, \end{aligned} \quad (12)$$

where $|A0\rangle$, $|A1\rangle$, and $|A2\rangle$ are orthogonal states of the ancilla. In Section IV B, we consider an implementation with SPM interactions and the initial ancilla state being photons in additional cavities. In Section IV C, we consider TLE interactions with the ancilla state being the TLE states.

B. One-Way Repeater with SPM Interactions

For our repeater implementation with SPM interactions to be as hardware-efficient as possible, we employ a three-mode RQPN with a two-step protocol, utilizing one ancillary cavity that is initialized in a single-photon Fock state, $|1_3\rangle$, at the beginning of each step, as illustrated in Figs. 3(a) and 3(b). The first step corrects for

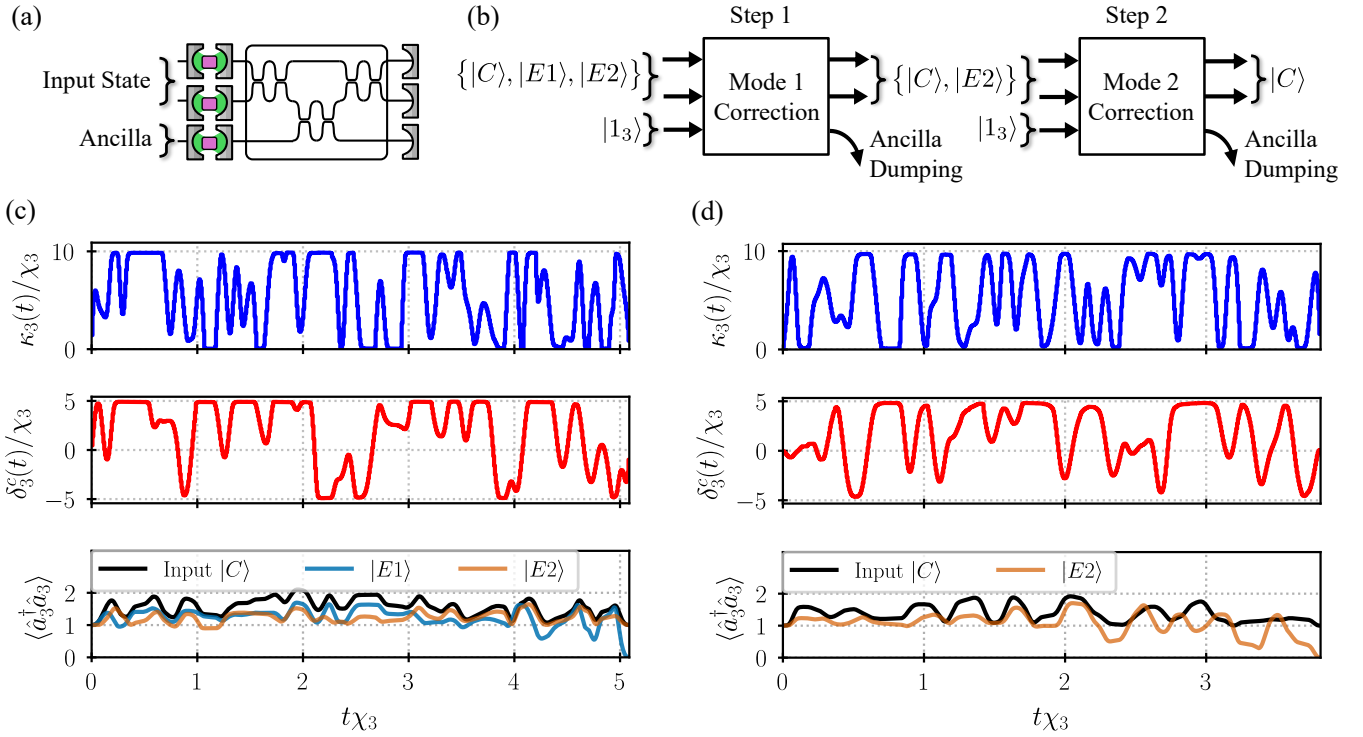


FIG. 3. Implementation of a measurement-free one-way quantum repeater using a three-mode RQPN with SPM interactions. (a) Modes 1 and 2 are used for the input state, and mode 3 contains the ancillary state. (b) The single-photon loss correction task is divided into two steps: the first corrects for loss in mode 1, and the second for loss in mode 2. Before each step, the ancilla cavity receives a single photon and is initialized to state $|1_3\rangle$. (c) Selected plots of the dynamics in step 1. The top and center panels plot the optimized waveguide coupling and detuning of the ancilla cavity ($m = 3$). The bottom panel plots the expectation value of the photon number operator for the three correctable input states for the example of $|\alpha|^2 = |\beta|^2 = 0.5$. (d) Selected plots of the dynamics in step 2. In the bottom panel, only the input states $|C\rangle$ and $|E2\rangle$ are relevant. Additional information for the optimization and result is in Supplemental Material SVI [41], Figs. 7 and 8.

photon loss in mode 1 by the transformation

$$\begin{aligned} \text{No loss : } & |C\rangle \otimes |1_3\rangle \rightarrow |C\rangle \otimes |1_3\rangle \\ \text{Mode 1 loss : } & |E1\rangle \otimes |1_3\rangle \rightarrow |C\rangle \otimes |0_3\rangle \\ \text{Mode 2 loss : } & |E2\rangle \otimes |1_3\rangle \rightarrow |E2\rangle \otimes |1_3\rangle. \end{aligned} \quad (13)$$

Before the second step, cavity 3 is emptied and re-initialized in the state $|1_3\rangle$, as illustrated in Fig. 3(b). Therefore, correcting for loss in mode 2 in the second step imparts the transformation

$$\begin{aligned} \text{No loss : } & |C\rangle \otimes |1_3\rangle \rightarrow |C\rangle \otimes |1_3\rangle \\ \text{Mode 2 loss : } & |E2\rangle \otimes |1_3\rangle \rightarrow |C\rangle \otimes |0_3\rangle. \end{aligned} \quad (14)$$

To simplify the optimization, we keep the coupling matrix fixed with values

$$\mathbf{C} = \begin{bmatrix} 0 & 1 & 1 \\ 1 & 0 & 1 \\ 1 & 1 & 0 \end{bmatrix}. \quad (15)$$

Note that the diagonal elements can be set to zero, since the self-coupling terms, $C_{mm}\kappa_m(t)$, in Eq. (1) may always be offset by shifting the detunings. Figures 3(c) and 3(d) plot the optimized controls and the expectation value of

the photon number operator for the ancillary cavity, illustrating the donation of a photon for input state $|E1\rangle$ (c) and $|E2\rangle$ (d). The corresponding process durations are $5.09/\chi_3$ for step 1 and $3.81/\chi_3$ for step 2. The duration of the full repeater task is $T = 8.90/\chi_3$, which is 4.5 and 7.1 times faster than the reported implementations in Refs. [24] and [25], respectively. We used $N_{\text{bin}} = 640$ and penalized the control bandwidths to obtain smooth signals at the expense of longer process duration (for instance, we found a solution with $T = 8.36/\chi_3$ without bandwidth penalty and $N_{\text{bin}} = 80$). Each transformation was optimized separately to achieve $\mathcal{I} < 0.05\%$, resulting in $\mathcal{I} = 0.08\%$ for the full two-step process.

C. One-Way Repeater with TLE Interactions

To implement a repeater with TLE interactions, we design a compact two-mode RQPN by using the TLEs as ancillary systems, as illustrated in Fig. 4(a). The TLEs are initialized in the excited state, $|e_m\rangle$ for $m = 1$ and 2. The TLE in cavity m donates a photon by relaxing to its ground state, if a photon is missing from mode m in the photonic input state. Thus, the repeater transformation

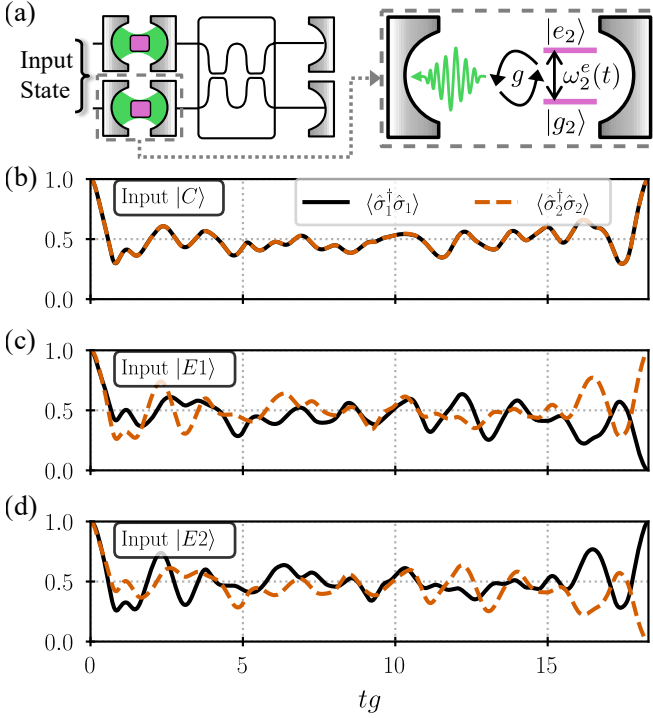


FIG. 4. Implementation of the measurement-free one-way quantum repeater using a two-mode RQPN with TLE interactions. (a) The input states are captured by the cavities, and the TLEs are used as ancillary systems by initializing them to their excited states, $|A0\rangle = |e_1\rangle|e_2\rangle$. (b)-(d) Plots of the evolution of the excited state probability of the two TLEs for input states $|C\rangle$ (b), $|E1\rangle$ (c), and $|E2\rangle$ (d). As in Fig. 3, we consider the example of $|\alpha|^2 = |\beta|^2 = 0.5$ in the input state. Additional information for the optimization and result, including optimized controls, is in Supplemental Material SVI [41], Fig. 9.

in Eq. (12) is implemented with ancillary states $|A0\rangle = |e_1\rangle|e_2\rangle$, $|A1\rangle = |g_1\rangle|e_2\rangle$, and $|A2\rangle = |e_1\rangle|g_2\rangle$. We use a fixed coupling matrix

$$\mathbf{C} = \begin{bmatrix} 0 & 1 \\ 1 & 0 \end{bmatrix}, \quad (16)$$

and optimize the cavity-waveguide couplings, cavity and TLE detunings, and time-bin durations. The resulting process duration is $T = 18.31/g$, which is 2.2 and 3.4 times faster than the reported implementations in Refs. [24] and [25]. Figures 4(b-d) plot the excited state probability of TLE 1 (black line) and 2 (orange line) for input states $|C\rangle$ (b), $|E1\rangle$ (c), and $|E2\rangle$ (d). It is clearly observed how TLE m donates a photon if a photon was lost from the corresponding input mode m . We used $N_{\text{bin}} = 640$ and penalized the control bandwidths to obtain smooth control signals and infidelity $\mathcal{I} < 0.1\%$.

One-Way Repeater Implementations			
Architecture	Duration	# Linear	# Nonlinear
RQPN (SPM)	$8.90/\chi_3$	3	3
RQPN (TLE)	$18.31/g$	1	2
Neural Network [25]	$62.83/\chi_3$	240	160
Three-mode cavities [24]	$40/\chi_2$	13	2

TABLE I. Comparison of one-way repeater implementations. The columns show the duration, T , the number of linear components, and the number of nonlinear elements.

D. Comparison of Architectures

Comparisons between different architectures require care, as they may rely on different material systems and pose different engineering challenges. Nevertheless, time and hardware efficiency may be compared using process durations in units of the inverse nonlinear interaction rate, $T = T_\eta/\Gamma_{\text{NL}}$, and the required numbers of linear and nonlinear components. In Ref. [24], second-order nonlinear interactions between two cavity modes, \hat{a} and \hat{b} , were used with the Hamiltonian: $\hat{H}_{\text{SHG}} = \hbar\chi_2(\hat{a}^\dagger\hat{b}\hat{b} + \hat{a}\hat{b}^\dagger\hat{b}^\dagger)$. The authors reported a one-way repeater duration of $40/\chi_2$ using 13 linear and 2 nonlinear components. In Ref. [25], SPM interactions were used, described by the transformation $\sum_n e^{i\phi n(n-1)} |n\rangle\langle n|$, with $\phi = \pi$. This transformation corresponds to a duration of $(\pi/2)/\chi_3$, when comparing to our SPM Hamiltonian in Eq. (3). The neural network architecture in Ref. [25] required 40 layers, each layer consisting of a linear mixing circuit followed by nonlinear interactions, to implement the one-way repeater, resulting in a duration of $62.8/\chi_3$, 240 linear and 160 nonlinear components. Table I summarizes these results along with the RQPN performance found in Sections IV B and IV C. The SPM-based RQPN and Ref. [25] use the same nonlinearity and thereby provide the clearest comparison. Table I shows that the RQPN is 7.1 times faster than the neural network architecture and reduces the component overhead by a factor of 80 (53.3) for linear (nonlinear) elements. Compared to the three-mode processor architecture in Ref. [24], the dimensionless duration, T_η , is 4.5 times shorter for the RQPN with SPM interactions. Even with TLE interactions, where the dynamics are more complex, the RQPN outperforms existing architectures in time efficiency by factors of 2.2 and 3.4, as seen from Table I, while using only one linear and two nonlinear components.

For each type of nonlinear interaction, we have found the ratio between the duration of RQPN implementations of the one-way repeater, T_{rep} , and the dual-rail qubit-qubit CZ gate, T_{CZ} . We obtain $T_{\text{rep}}/T_{CZ} = 11.5$ and 4.6 for SPM and TLE interactions, respectively. Given the added complexity of implementing the one-way repeater relative to the CZ gate, these small ratios underscore the potential benefit of direct transformations over single-

and two-qubit decompositions. Furthermore, this benefit is significantly larger for the implementation with TLEs compared to SPM interactions.

Proposals of spatially distributed architectures relying on nonlinearities from three-level Λ -systems are found in, e.g., Refs. [27, 58]. Their advantage stems from the possibility of using passive nonlinear elements, though circulators are required, and, in some cases, phase-conjugating mirrors to provide time-reversal of wave packets [27]. Importantly, avoiding fidelity degradation due to wave-packet distortion in passive three-level system interactions requires that the pulse bandwidths be significantly smaller than the light-matter coupling rate, Γ_{NL} . Since spatially distributed nonlinear elements must be traversed sequentially in these architectures, the duration of each layer must be significantly longer than $1/\Gamma_{NL}$. This requirement severely limits the achievable process duration. In contrast, the RQPN architecture does not restrict any system process to be slower than $1/\Gamma_{NL}$. Furthermore, the effective circuit depth of the RQPN is determined by the duration of the control signals, which can be easily reprogrammed without requiring hardware modifications. Additionally, circulators are straightforwardly avoided by connecting the nonlinear cavities to the input-output channels via, e.g., fast multiport routers [32].

A proposal for a minimal-resource architecture is found in Ref. [59]. It utilizes a single nonlinear element and a storage channel to enable counter-propagating wave packets to interact sequentially. With the RQPN architecture, we combine the hardware efficiency of reusing physical elements [59] with the time efficiency of parallel processing across multiple spatial channels [25–27, 58].

V. TOWARDS EXPERIMENTAL REALIZATIONS

We consider Pockels materials, such as lithium niobate [60], lithium tantalate [61], or barium titanate [62], to be the most promising platforms for realizing fast, low-loss control over cavity resonances [63, 64] and waveguide couplings [31, 65–67]. Scalable electrical control via flip-chip bonding to complementary metal-oxide-semiconductor (CMOS) microchips [68] is possible with low-voltage device designs [64, 69]. Pulse trapping was achieved in relatively large ring resonator structures [31, 70], and Ref. [67] describes progress towards trapping in smaller photonic crystal cavities, which enable larger nonlinear coupling rates when integrated with quantum emitters.

In our view, it remains an open question which non-

linear material platform is best suited for RQPN implementations. The bulk $\chi^{(2)}$ nonlinearity of lithium niobate was demonstrated to reach a nonlinear interaction rate of $\chi_2 \sim 1\text{MHz}$ [71], which is a factor of six smaller than the smallest demonstrated intrinsic loss rate of integrated ring resonators [72]. While further improvements may push the coupling-to-loss ratio into the strong coupling regime, it is likely that other materials will be needed. Heterogeneous integration is a promising approach to combine a controllable integrated circuit with highly nonlinear materials, including 2D materials [73], carbon nanotubes [74], III-V quantum dots [75], hot atomic vapors [76], and trapped atoms [77]. The key metric for comparing material systems is cooperativity (coupling-to-decoherence ratio), along with integrability and scalability.

VI. CONCLUSION AND OUTLOOK

In conclusion, we have proposed the RQPN architecture for deterministic photonic QIP and demonstrated its ability to reduce the processing speed of direct implementations of multi-qubit transformations compared to single- and two-qubit decompositions. Importantly, we have demonstrated substantial improvements in both time and hardware efficiency relative to state-of-the-art architectures by considering single-photon loss correction, which is a key QIP functionality.

We addressed the challenge of loss and decoherence by minimizing the durations of QIP tasks. In future work, we anticipate further improvements in understanding and performance by explicitly incorporating these error mechanisms into the optimization procedure.

CODE AVAILABILITY

The data and code that support the findings of this article are openly available in Ref. [78].

ACKNOWLEDGMENTS

We thank Stefan Krastanov for many helpful conversations. This work was supported by the Villum Foundation (QNET-NODES, Grant No. 37417), Innovation Fund Denmark (EQUAL, Grant No. 4356-00007B), and the Danish National Research Foundation (NanoPhoton, Grant No. DNRF147).

[1] H. J. Kimble, *Nature* **453**, 1023 (2008).
[2] M. A. Nielsen and I. L. Chuang, *Quantum Computation and Quantum Information* (Cambridge University Press, 2010).
[3] P. Kok, W. J. Munro, K. Nemoto, T. C. Ralph, J. P. Dowling, and G. J. Milburn, *Rev. Mod. Phys.* **79**, 135

(2007).

[4] E. Knill, R. Laflamme, and G. J. Milburn, *Nature* **409**, 46 (2001).

[5] S. Bartolucci, P. Birchall, H. Bombín, H. Cable, C. Dawson, M. Gimeno-Segovia, E. Johnston, K. Kieling, N. Nickerson, M. Pant, F. Pastawski, T. Rudolph, and C. Sparrow, *Nature Communications* **14**, 912 (2023).

[6] J. H. Shapiro, *Phys. Rev. A* **73**, 062305 (2006).

[7] J. Gea-Banacloche, *Phys. Rev. A* **81**, 043823 (2010).

[8] S. Xu, E. Rephaeli, and S. Fan, *Phys. Rev. Lett.* **111**, 223602 (2013).

[9] A. Nysteen, D. P. S. McCutcheon, M. Heuck, J. Mørk, and D. R. Englund, *Phys. Rev. A* **95**, 062304 (2017).

[10] S. Slussarenko and G. J. Pryde, *Applied Physics Reviews* **6**, 041303 (2019).

[11] K. Xia, M. Johnsson, P. L. Knight, and J. Twamley, *Phys. Rev. Lett.* **116**, 023601 (2016).

[12] B. Viswanathan and J. Gea-Banacloche, *Phys. Rev. A* **97**, 032314 (2018).

[13] T. Levy-Yeyati, C. Vega, T. Ramos, and A. González-Tudela, *PRX Quantum* **6**, 010342 (2025).

[14] D. J. Brod and J. Combes, *Phys. Rev. Lett.* **117**, 080502 (2016).

[15] T. C. Ralph, I. Söllner, S. Mahmoodian, A. G. White, and P. Lodahl, *Phys. Rev. Lett.* **114**, 173603 (2015).

[16] F. Yang, M. M. Lund, T. Pohl, P. Lodahl, and K. Mølmer, *Phys. Rev. Lett.* **128**, 213603 (2022).

[17] M. Heuck, K. Jacobs, and D. R. Englund, *Phys. Rev. A* **101**, 042322 (2020).

[18] M. Heuck, K. Jacobs, and D. R. Englund, *Phys. Rev. Lett.* **124**, 160501 (2020).

[19] S. Krastanov, K. Jacobs, G. Gilbert, D. R. Englund, and M. Heuck, *npj Quantum Information* **8**, 103 (2022).

[20] R. J. Thompson, G. Rempe, and H. J. Kimble, *Phys. Rev. Lett.* **68**, 1132 (1992).

[21] K. Hennessy, A. Badolato, M. Winger, D. Gerace, M. Atatüre, S. Gulde, S. Fält, E. L. Hu, and A. Imamoğlu, *Nature* **445**, 896 (2007).

[22] P. Lodahl, *Quantum Science and Technology* **3**, 013001 (2017).

[23] Y. Ota, D. Takamiya, R. Ohta, H. Takagi, N. Kumagai, S. Iwamoto, and Y. Arakawa, *Applied Physics Letters* **112**, 093101 (2018).

[24] S. Krastanov, M. Heuck, J. H. Shapiro, P. Narang, D. R. Englund, and K. Jacobs, *Nature Communications* **12**, 191 (2021).

[25] G. R. Steinbrecher, J. P. Olson, D. Englund, and J. Carolan, *npj Quantum Information* **5**, 60 (2019).

[26] J. Ewaniuk, J. Carolan, B. J. Shastri, and N. Rotenberg, *Advanced Quantum Technologies* **6**, 2200125 (2023).

[27] J. R. Basani, M. Y. Niu, and E. Waks, *npj Quantum Information* **11**, 142 (2025).

[28] Y. Tanaka, J. Upham, T. Nagashima, T. Sugiya, T. Asano, and S. Noda, *Nature Materials* **6**, 862 (2007).

[29] Q. Xu, P. Dong, and M. Lipson, *Nature Physics* **3**, 406 (2007).

[30] M. Nakadai, T. Asano, and S. Noda, *Nature Photonics* **16**, 113 (2022).

[31] M. Zhang, C. Wang, Y. Hu, A. Shams-Ansari, T. Ren, S. Fan, and M. Lončar, *Nature Photonics* **13**, 36 (2019).

[32] M. Heuck, in *Conference on Lasers and Electro-Optics/Europe (CLEO/Europe 2023) and European Quantum Electronics Conference (EQEC 2023)* (Optica Publishing Group, 2023) p. ci_1-5.

[33] I. L. Chuang, D. W. Leung, and Y. Yamamoto, *Phys. Rev. A* **56**, 1114 (1997).

[34] M. H. Michael, M. Silveri, R. T. Brierley, V. V. Albert, J. Salmilehto, L. Jiang, and S. M. Girvin, *Phys. Rev. X* **6**, 031006 (2016).

[35] J. Gough and M. R. James, *Communications in Mathematical Physics* **287**, 1109 (2009).

[36] J. Gough and M. R. James, *IEEE Transactions on Automatic Control* **54**, 2530 (2009).

[37] J. Combes, J. Kerckhoff, and M. Sarovar, *Advances in Physics: X* **2**, 784 (2017).

[38] C. W. Gardiner and M. J. Collett, *Phys. Rev. A* **31**, 3761 (1985).

[39] C. Gardiner and P. Zoller, *Quantum Noise: A Handbook of Markovian and Non-Markovian Quantum Stochastic Methods with Applications to Quantum Optics*, Springer Series in Synergetics (Springer, 2004).

[40] M. Bundgaard-Nielsen, D. Englund, M. Heuck, and S. Krastanov, *Quantum* **9**, 1710 (2025).

[41] See Supplementary Material at [...] for details, which includes Ref. 79.

[42] M. Reck, A. Zeilinger, H. J. Bernstein, and P. Bertani, *Phys. Rev. Lett.* **73**, 58 (1994).

[43] W. R. Clements, P. C. Humphreys, B. J. Metcalf, W. S. Kolthammer, and I. A. Walmsley, *Optica* **3**, 1460 (2016).

[44] E. Jaynes and F. Cummings, *Proceedings of the IEEE* **51**, 89 (1963).

[45] T. Propson, B. E. Jackson, J. Koch, Z. Manchester, and D. I. Schuster, *Phys. Rev. Appl.* **17**, 014036 (2022).

[46] M. H. Goerz, S. C. Carrasco, and V. S. Malinovsky, *Quantum* **6**, 871 (2022).

[47] A. J. Goldschmidt, J. L. DuBois, S. L. Brunton, and J. N. Kutz, *Quantum* **6**, 837 (2022).

[48] P. Guilmot, A. Bocquet, É. Genois, D. Weiss, and R. Gautier (2025).

[49] J. Bradbury, R. Frostig, P. Hawkins, M. J. Johnson, C. Leary, D. Maclaurin, G. Necula, A. Paszke, J. Vander-Plas, S. Wanderman-Milne, and Q. Zhang, *JAX: composable transformations of Python+NumPy programs* (2018).

[50] I. Goodfellow, Y. Bengio, and A. Courville, *Deep Learning* (MIT Press, 2016) <http://www.deeplearningbook.org>.

[51] T. C. Ralph, K. J. Resch, and A. Gilchrist, *Phys. Rev. A* **75**, 022313 (2007).

[52] E. T. Campbell, B. M. Terhal, and C. Vuillot, *Nature* **549**, 172 (2017).

[53] D. Aharonov and M. Ben-Or, *SIAM Journal on Computing* **38**, 1207 (2008).

[54] R. Acharya, D. A. Abanin, L. Aghababaie-Beni, I. Aleiner, T. I. Andersen, M. Ansmann, F. Arute, K. Arya, A. Asfaw, N. Astrakhantsev, *et al.* (Google Quantum AI and Collaborators), *Nature* **638**, 920 (2025).

[55] M. L. Chan, A. A. Capatos, P. Lodahl, A. S. Sørensen, and S. Paesani, *Practical blueprint for low-depth photonic quantum computing with quantum dots* (2025), arXiv:2507.16152 [quant-ph].

[56] S. Muralidharan, J. Kim, N. Lütkenhaus, M. D. Lukin, and L. Jiang, *Phys. Rev. Lett.* **112**, 250501 (2014).

[57] F. M. Miatto, M. Epping, and N. Lütkenhaus, *Quantum* **2**, 75 (2018).

[58] B. Bartlett and S. Fan, *Phys. Rev. A* **101**, 042319 (2020).

[59] B. Bartlett, A. Dutt, and S. Fan, *Optica* **8**, 1515 (2021).

[60] D. Zhu, L. Shao, M. Yu, R. Cheng, B. Desiatov, C. J. Xin, Y. Hu, J. Holzgrafe, S. Ghosh, A. Shams-Ansari, E. Puma, N. Sinclair, C. Reimer, M. Zhang, and M. Lončar, *Adv. Opt. Photon.* **13**, 242 (2021).

[61] C. Wang, Z. Li, J. Riemensberger, G. Lihachev, M. Churaev, W. Kao, X. Ji, J. Zhang, T. Blesin, A. Davydova, Y. Chen, K. Huang, X. Wang, X. Ou, and T. J. Kippenberg, *Nature* **629**, 784 (2024).

[62] D. Chelladurai, M. Kohli, J. Winiger, D. Moor, A. Messner, Y. Fedoryshyn, M. Eleraky, Y. Liu, H. Wang, and J. Leuthold, *Nature Materials* **24**, 868 (2025).

[63] M. Li, J. Ling, Y. He, U. A. Javid, S. Xue, and Q. Lin, *Nature Communications* **11**, 4123 (2020).

[64] H. Larocque, D. L. P. Vitullo, A. Sludds, H. Sattari, I. Christen, G. Choong, I. Prieto, J. Leo, H. Zarebidaki, S. Lohani, B. T. Kirby, Ö. Soykal, M. Soltani, A. H. Ghadimi, D. R. Englund, and M. Heuck, *ACS Photonics* **11**, 3860 (2024), publisher: American Chemical Society.

[65] Y. Xue, R. Gan, K. Chen, G. Chen, Z. Ruan, J. Zhang, J. Liu, D. Dai, C. Guo, and L. Liu, *Optica* **9**, 1131 (2022).

[66] J. F. Herrmann, D. J. Dean, C. J. Sarabalis, V. Ansari, K. Multani, E. A. Wollack, T. P. McKenna, J. D. Witmer, and A. H. Safavi-Naeini, *Opt. Express* **32**, 6168 (2024).

[67] M. Rasmussen, H. Zarebidaki, H. Sattari, A. H. Ghadimi, M. Zahidy, M. Galili, D. Englund, D. L. Vitullo, and M. Heuck, in *Optica Quantum 2.0 Conference and Exhibition* (Optica Publishing Group, 2025) p. QM4B.4.

[68] S. Daudlin, A. Rizzo, S. Lee, D. Khilwani, C. Ou, S. Wang, A. Novick, V. Gopal, M. Cullen, R. Parsons, K. Jang, A. Molnar, and K. Bergman, *Nature Photonics* **19**, 502 (2025).

[69] C. Wang, M. Zhang, X. Chen, M. Bertrand, A. Shams-Ansari, S. Chandrasekhar, P. Winzer, and M. Lončar, *Nature* **562**, 101 (2018).

[70] X. Li, Y. Hu, T. Ge, A. Cordaro, Y. Song, X. Zhu, S. Lu, K. Powell, L. Magalhães, U. Senica, N. Sinclair, and M. Lončar, *Spectral-temporal processing using integrated recursive electro-optic circuit* (2025), arXiv:2509.25102 [physics.optics].

[71] J. Lu, M. Li, C.-L. Zou, A. A. Sayem, and H. X. Tang, *Optica* **7**, 1654 (2020).

[72] X. Zhu, Y. Hu, S. Lu, H. K. Warner, X. Li, Y. Song, L. M. aes, A. Shams-Ansari, A. Cordaro, N. Sinclair, and M. Lončar, *Photon. Res.* **12**, A63 (2024).

[73] F. J. G. de Abajo, D. N. Basov, F. H. L. Koppens, L. Orsini, M. Ceccanti, S. Castilla, L. Cavicchi, M. Polini, P. A. D. Gonçalves, A. T. Costa, N. M. R. Peres, *et al.*, *ACS Photonics* **12**, 3961 (2025).

[74] A. P. Ovyyan, M.-K. Li, H. Gehring, F. Beutel, S. Kumar, F. Hennrich, L. Wei, Y. Chen, F. Pyatkov, R. Krupke, and W. H. P. Pernice, *Nature Communications* **14**, 3933 (2023).

[75] S. Aghaeimeibodi, B. Desiatov, J.-H. Kim, C.-M. Lee, M. A. Buyukkaya, A. Karasahin, C. J. K. Richardson, R. P. Leavitt, M. Lončar, and E. Waks, *Applied Physics Letters* **113**, 221102 (2018).

[76] R. Zektzer, X. Lu, K. T. Hoang, R. Shrestha, S. Austin, F. Zhou, A. Chanana, G. Holland, D. Westly, P. Lett, A. V. Gorshkov, and K. Srinivasan, *Optica* **11**, 1376 (2024).

[77] X. Zhou, H. Tamura, T.-H. Chang, and C.-L. Hung, *Phys. Rev. X* **14**, 031004 (2024).

[78] "An open-source implementation of the numerical optimization of recirculating quantum photonic networks", <https://github.com/EmilGrovn/RecirculatingQuantumPhotonicNetworks>.

[79] M. Houde, W. McCutcheon, and N. Quesada, *Canadian Journal of Physics* **102**, 497 (2024).

Supplemental Material for "Recirculating Quantum Photonic Networks for Fast Deterministic Quantum Information Processing"

SI. DERIVATION OF THE HAMILTONIAN

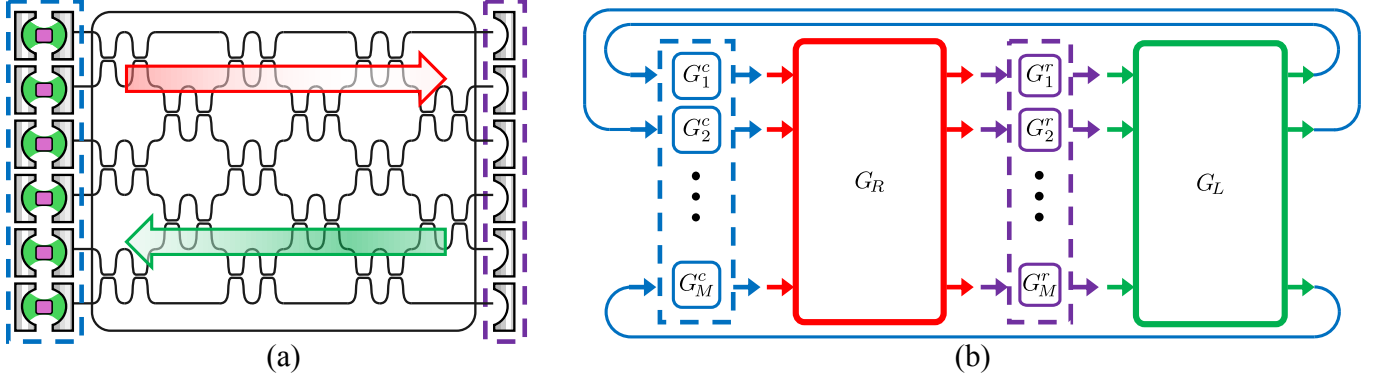


FIG. S1. (a) Schematic illustration of the RQPN divided into blocks used to derive the Hamiltonian. (b) Corresponding SLH block diagram. Following photons through the RQPN, they start in the nonlinear cavities (blue), travel left-to-right through the linear mixing circuit (red), are reflected by the mirrors (purple), and travel back through the mixing circuit (green). The fields after one round trip are then the inputs to the nonlinear cavities, as illustrated using the lines connecting the green and blue blocks.

We use the SLH formalism [S1–S3] to describe the dynamics of the recirculating quantum photonic network (RQPN) in its recirculating configuration, shown in Fig. S1(a). The SLH formalism is a framework for describing systems composed of localized quantum systems and linear scattering components, connected by itinerant bosonic quantum fields [S3]. Each subsystem in the SLH formalism is described by a triplet $G = (\mathbf{S}, \hat{\mathbf{L}}, \hat{H})$ to model a localized quantum system with M input-output channels for itinerant fields. The Hamiltonian, \hat{H} , describes the internal degrees of freedom of the subsystem. The Lindblad operator, $\hat{\mathbf{L}}$, is an $M \times 1$ vector of operators, describing the coupling from the quantum system into the outgoing bosonic fields. The scattering matrix, \mathbf{S} , is an $M \times M$ unitary matrix which describes the direct scattering between incoming and outgoing itinerant fields. The SLH formalism provides a set of rules for connecting subsystems into larger systems, which are also described by a single triplet, G , thereby enabling modularity and simplifying calculations of the full system dynamics.

In Fig. S1(a), we have divided the RQPN into components, and Fig. S1(b) shows the corresponding SLH block diagram used to derive the full-system triplet, G . Going from left to right, we follow the path photons take on a round trip through the recirculating circuit. The nonlinear cavities are presented by blocks $G_m^c = (1, \sqrt{\kappa_m(t)}\hat{a}_m, \hat{H}_m)$, $m = 1, 2, \dots, M$. The outputs of the cavities (blue arrows) couple to the right-propagating fields in the linear mixing circuit, which is represented by $G_R = (\mathbf{S}_R, 0, 0)$ (red arrows). The right-propagating fields are coupled to the left-propagating fields by reflection off the mirrors that are represented by G_m^r . Note that we, without loss of generality, assume that the mirrors do not impart any relative phase-shifts on the fields, so $G_m^r = (\mathbf{I}, 0, 0)$ (where \mathbf{I} is the $M \times M$ identity matrix) is left out of the analysis below. Finally, the left-propagating fields are transformed by the linear mixing circuit $G_L = (\mathbf{S}_L^T, 0, 0)$ (green arrow) and are coupled back into the nonlinear cavities, thus forming a closed circuit as indicated by the arrows connecting G_L and G_m^c .

We use the SLH composition rules, introduced in section 5.4 of Ref. [S3], to derive the triplet and thus the Hamiltonian of the RQPN in its recirculating configuration. First, we describe the cavities as one block with M input-output ports (dashed blue box) using the so-called concatenation rule [S3]:

$$G_{\text{cav}} = \left(\mathbf{I}, \begin{bmatrix} \sqrt{\kappa_1(t)}\hat{a}_1 \\ \sqrt{\kappa_2(t)}\hat{a}_2 \\ \dots \\ \sqrt{\kappa_M(t)}\hat{a}_M \end{bmatrix}, \sum_{m=1}^M \hat{H}_m \right). \quad (\text{S1})$$

The blocks represented by G_{cav} , G_R , and G_L are then connected using the cascading rule, $G_2 \triangleleft G_1 = (\mathbf{S}_2 \mathbf{S}_1, \hat{\mathbf{L}}_2 + \mathbf{S}_2 \hat{\mathbf{L}}_1, \hat{H}_1 + \hat{H}_2)$, for $G_2 = (\mathbf{S}_2, \hat{\mathbf{L}}_2, \hat{H}_2)$ and $G_1 = (\mathbf{S}_1, \hat{\mathbf{L}}_1, \hat{H}_1)$. We obtain the following triplet for the chain of

blocks:

$$\begin{aligned} G_{\text{chain}} &= G_L \triangleleft G_R \triangleleft G_{\text{cav}} = (\mathbf{S}_R^T, 0, 0) \triangleleft (\mathbf{S}_R, 0, 0) \triangleleft (I, \hat{\mathbf{L}}, \sum_m \hat{H}_m) = \\ &(\mathbf{S}_R^T \mathbf{S}_R, 0, 0) \triangleleft (I, \hat{\mathbf{L}}, \sum_m \hat{H}_m) = (\mathbf{S}_{RL}, \mathbf{S}_{RL} \hat{\mathbf{L}}, \sum_m \hat{H}_m), \quad \mathbf{S}_{RL} = \mathbf{S}_R^T \mathbf{S}_R \end{aligned} \quad (\text{S2})$$

The outputs of the chain are connected to its inputs, which can be described by the feedback reduction rule. In this special case, the circuit becomes closed, i.e., there is no coupling $\hat{\mathbf{L}}$ between the localized system and its surroundings. The Hamiltonian, as dictated by the feedback reduction rule [S3], is:

$$\hat{H}_{\text{RQPN}} = \sum_m \hat{H}_m + \frac{\hbar}{2i} \left((\mathbf{S}_{RL} \hat{\mathbf{L}})^\dagger \mathbf{S}_{RL} (I - \mathbf{S}_{RL})^{-1} \mathbf{S}_{RL} \hat{\mathbf{L}} - \text{H.C.} \right), \quad (\text{S3})$$

where H.C. is the hermitian conjugate of the term to the left of it. We can simplify the coupling term significantly. We use that \mathbf{S}_{RL} is unitary ($\mathbf{S}_{RL}^\dagger \mathbf{S}_{RL} = \mathbf{I}$) and that the matrices $(I - \mathbf{S}_{RL})^{-1}$ and \mathbf{S}_{RL} commute:

$$(\mathbf{S}_{RL} \hat{\mathbf{L}})^\dagger \mathbf{S}_{RL} (I - \mathbf{S}_{RL})^{-1} \mathbf{S}_{RL} \hat{\mathbf{L}} = \hat{\mathbf{L}}^\dagger \mathbf{S}_{RL}^\dagger \mathbf{S}_{RL} (I - \mathbf{S}_{RL})^{-1} \mathbf{S}_{RL} \hat{\mathbf{L}} = \hat{\mathbf{L}}^\dagger \mathbf{S}_{RL} (I - \mathbf{S}_{RL})^{-1} \hat{\mathbf{L}}.$$

We thus obtain a compact expression for the Hamiltonian:

$$\hat{H}_{\text{RQPN}} = \sum_m \hat{H}_m + \hbar \hat{\mathbf{L}}^\dagger \mathbf{C} \hat{\mathbf{L}}, \quad (\text{S4})$$

For $\sum_m H_m = \hbar \sum_m \delta_m^c(t) \hat{a}_m^\dagger \hat{a}_m + \hat{H}_{\text{NL}}$, the RQPN Hamiltonian in Eq. (S4) is the Hamiltonian in Eq. (10) in the main text:

$$\hat{H}(t) = \hbar \sum_m \delta_m^c(t) \hat{a}_m^\dagger \hat{a}_m + \hbar \sum_{n,m} C_{nm} \sqrt{\kappa_n^*(t) \kappa_m(t)} \hat{a}_n^\dagger \hat{a}_m + \hat{H}_{\text{NL}}.$$

We see that \mathbf{C} determines the coupling coefficient between the cavity modes. The coupling matrix, \mathbf{C} , is given by:

$$\mathbf{C} = \frac{\mathbf{M} - \mathbf{M}^\dagger}{2i}, \quad \mathbf{M} = \mathbf{S}_{RL} (I - \mathbf{S}_{RL})^{-1}, \quad \mathbf{S}_{RL} = \mathbf{S}_R^T \mathbf{S}_R, \quad (\text{S5})$$

where we require that all eigenvalues of \mathbf{S}_{RL} are different from 1, so $I - \mathbf{S}_{RL}$ is invertible. The matrix, $\mathbf{S}_{RL} = \mathbf{S}_R^T \mathbf{S}_R$, is symmetric and unitary. It follows that $\mathbf{M} = \mathbf{M}^T$, and thus $\mathbf{M}^\dagger = \mathbf{M}^*$. Evidently, the elements of \mathbf{C} are real and \mathbf{C} is symmetric.

SII. PROOF THAT COUPLING MATRIX \mathbf{C} CAN BE ANY SYMMETRIC REAL MATRIX

In the following, we prove that \mathbf{C} , Eq. (S5), can be any real symmetric matrix with finite eigenvalues. Let \mathbf{C} be a real symmetric matrix with finite eigenvalues. Then $\mathbf{C}^T \mathbf{C} = \mathbf{C} \mathbf{C}^T$, so by the spectral theorem we can write \mathbf{C} as [S4]:

$$\mathbf{C} = \mathbf{O} \text{diag}(\lambda_1, \dots, \lambda_M) \mathbf{O}^T, \quad (\text{S6})$$

where $\text{diag}(\lambda_1, \dots, \lambda_M)$ denotes a diagonal matrix with real eigenvalues λ_n for $n = 1, 2, \dots, M$, and \mathbf{O} is a real orthogonal matrix: $\mathbf{O} \mathbf{O}^T = \mathbf{O}^T \mathbf{O} = \mathbf{I}$. Since λ_n is a real number, we can write each eigenvalue as $\lambda_n = \cot(\theta_n/2)/2$ where $\theta_n \in [-\pi, 0] \cup [0, \pi]$, i.e., we ensure $\theta_n \neq 0$ to avoid infinite λ_n . We obtain:

$$\mathbf{C} = \mathbf{O} \text{diag} \left(\frac{1}{2} \cot(\theta_1/2), \dots, \frac{1}{2} \cot(\theta_M/2) \right) \mathbf{O}^T, \quad (\text{S7})$$

This parameterization of the eigenvalues is insightful, because we can calculate

$$\frac{1}{2} \cot(\theta_n/2) = \text{Im} \left\{ \frac{e^{i\theta_n}}{1 - e^{i\theta_n}} \right\}. \quad (\text{S8})$$

We can thus write \mathbf{C} in Eq. (S7) as

$$\mathbf{C} = \text{Im} \{ \mathbf{U}(\mathbf{I} - \mathbf{U})^{-1} \}, \quad (\text{S9})$$

where

$$\mathbf{U} = \mathbf{O} \text{diag} (e^{i\theta_1}, \dots, e^{i\theta_M}) \mathbf{O}^T. \quad (\text{S10})$$

We can verify that Eq. (S7) and Eq. (S9) are the same by inserting Eq. (S10) into Eq. (S9) and using the relation in Eq. (S8):

$$\begin{aligned} \mathbf{C} &= \text{Im} \left\{ \mathbf{O} \text{diag} (e^{i\theta_1}, \dots, e^{i\theta_M}) \mathbf{O}^T \left(\mathbf{I} - \mathbf{O} \text{diag} (e^{i\theta_1}, \dots, e^{i\theta_M}) \mathbf{O}^T \right)^{-1} \right\} \\ &= \text{Im} \left\{ \mathbf{O} \text{diag} (e^{i\theta_1}, \dots, e^{i\theta_M}) \mathbf{O}^T \left(\mathbf{O} (\mathbf{I} - \text{diag} (e^{i\theta_1}, \dots, e^{i\theta_M})) \mathbf{O}^T \right)^{-1} \right\} \\ &= \text{Im} \left\{ \mathbf{O} \text{diag} (e^{i\theta_1}, \dots, e^{i\theta_M}) \mathbf{O}^T \mathbf{O} \left((\mathbf{I} - \text{diag} (e^{i\theta_1}, \dots, e^{i\theta_M})) \right)^{-1} \mathbf{O}^T \right\} \\ &= \text{Im} \left\{ \mathbf{O} \text{diag} (e^{i\theta_1}, \dots, e^{i\theta_M}) \left(\text{diag} (1 - e^{i\theta_1}, \dots, 1 - e^{i\theta_M}) \right)^{-1} \mathbf{O}^T \right\} \\ &= \mathbf{O} \text{Im} \left\{ \text{diag} (e^{i\theta_1}, \dots, e^{i\theta_M}) \text{diag} \left(\frac{1}{1 - e^{i\theta_1}}, \dots, \frac{1}{1 - e^{i\theta_M}} \right) \right\} \mathbf{O}^T \\ &= \mathbf{O} \text{Im} \left\{ \text{diag} \left(\frac{e^{i\theta_1}}{1 - e^{i\theta_1}}, \dots, \frac{e^{i\theta_M}}{1 - e^{i\theta_M}} \right) \right\} \mathbf{O}^T \\ &= \mathbf{O} \text{diag} \left(\frac{1}{2} \cot(\theta_1/2), \dots, \frac{1}{2} \cot(\theta_M/2) \right) \mathbf{O}^T, \end{aligned}$$

where at the second equal sign, we used that $\mathbf{O}\mathbf{O}^T = \mathbf{I}$. At the third equal sign, we used that $\mathbf{O}^{-1} = \mathbf{O}^T$ for a real orthogonal matrix \mathbf{O} . At the fourth equal sign, we used that $\mathbf{O}\mathbf{O}^T = \mathbf{I}$ and gathered the two diagonal matrix terms. At the fifth equal sign, we calculated the inverted diagonal matrix and used that \mathbf{O} is real, i.e., $\mathbf{O}^\dagger = \mathbf{O}^T$. This means that $\text{Im}\{\mathbf{O}\mathbf{A}\mathbf{O}^T\} = \mathbf{O} \text{Im}\{\mathbf{A}\} \mathbf{O}^T$, which we used. At the sixth equal sign, we calculated the product of the two diagonal matrices. At the last equal sign, we invoked the relation in Eq. (S8) element-wise and obtained exactly the expression for \mathbf{C} in Eq. (S7). We note that \mathbf{U} in Eq. (S10) is a symmetric unitary matrix with eigenvalues different from 1, since $\theta_n \in [-\pi, 0] \cup [0, \pi]$. By Takagi factorization, there exists a unitary matrix \mathbf{S}_R such that $\mathbf{U} = \mathbf{S}_R^T \mathbf{S}_R$ [S4]. Setting $\mathbf{S}_R^T \mathbf{S}_R = \mathbf{U}$ in the definition of the coupling matrix, Eq. (S5), yields exactly the matrix in Eq. (S9), which equals Eq. (S7) by the calculation above. We have thus shown that the coupling matrix can be any real symmetric matrix with finite eigenvalues.

SIII. NUMERICAL FRAMEWORK

In the following sections, we provide further details on the numerical framework used to calculate the dynamics of the RQPN states and optimize the controls.

A. Parameterization of Controls

As explained in the main text, we parameterize the control signals as piece-wise constant with N_{bin} time bins, so the evolution in time is:

$$|\psi(T)\rangle = \left(\hat{U}_{N_{\text{bin}}} \dots \hat{U}_2 \hat{U}_1 \right) |\psi_{\text{in}}\rangle, \quad \hat{U}_p = \exp \left(\frac{-i\hat{H}_p \Delta t_p}{\hbar} \right), \quad (\text{S11})$$

where \hat{H}_p is the Hamiltonian and Δt_p is the duration of time bin p . We note that the above is mathematically equivalent to a time evolution with unit time steps (so the renormalized time is in the interval $[0, N_{\text{bin}}]$) with renormalized Hamiltonians of each unit time bin $\hat{h} = [\hat{H}_1 \Delta t_1, \hat{H}_2 \Delta t_2, \dots, \hat{H}_P \Delta t_p]$, as the authors use in Ref. [S5]. This renormalized time evolution allows us to directly optimize not only the rates (and \mathbf{C}), but also the time bin durations, Δt_p , and thereby the total physical duration $T = \sum_{p=1}^{N_{\text{bin}}} \Delta t_p$.

We normalize parameters with units of time or frequency using the nonlinear interaction rate Γ_{NL} (either $\Gamma_{\text{NL}} = \chi_3$ or $\Gamma_{\text{NL}} = g$). The Hamiltonian of each time bin p is

$$\hat{h}_p/(\hbar\Gamma_{\text{NL}}) = \frac{\hat{H}_p\Delta t_p}{\hbar\Gamma_{\text{NL}}} = \sum_m \frac{\delta_{m,p}^c}{\Gamma_{\text{NL}}} \hat{a}_m^\dagger \hat{a}_m + \frac{\hat{H}_{\text{NL},p}\Delta t_p}{\hbar\Gamma_{\text{NL}}} + \sum_{n,m} C_{nm} \sqrt{\frac{\kappa_{n,p}^*}{\Gamma_{\text{NL}}} \frac{\kappa_{m,p}}{\Gamma_{\text{NL}}}} \hat{a}_n^\dagger \hat{a}_m, \quad (\text{S12})$$

where the nonlinear Hamiltonian when using self-phase modulation (SPM), $\Gamma_{\text{NL}} = \chi_3$, is:

$$\frac{\hat{H}_{\text{NL},p}\Delta t_p}{\hbar\chi_3} = -\Delta t_p \sum_m \hat{a}_m^\dagger \hat{a}_m^\dagger \hat{a}_m \hat{a}_m, \quad (\text{S13})$$

while, when using two-level emitters (TLEs) with $\Gamma_{\text{NL}} = g$, the optically nonlinear Hamiltonian is:

$$\frac{\hat{H}_{\text{NL},p}\Delta t_p}{\hbar g} = \Delta t_p \left(\sum_m \hat{a}_m \sigma_m^\dagger + \hat{a}_m^\dagger \sigma_m \right) + \sum_m \frac{\delta_{m,p}^e}{g} \hat{\sigma}_m^\dagger \hat{\sigma}_m. \quad (\text{S14})$$

Each index of the sums runs from 1 to M . We have absorbed the factor of Δt_p into the parameters $\delta_{m,p}$, $\kappa_{m,p}$, and $\delta_{m,p}^e$, so the physical detunings and coupling are given by

$$\delta_m^c(t_p) = \delta_{m,p}^c/\Delta t_p, \quad \delta_m^e(t_p) = \delta_{m,p}^e/\Delta t_p, \quad \kappa_m(t_p) = \kappa_{m,p}/\Delta t_p, \quad t_p \in \left[\sum_{q=1}^{p-1} \Delta t_q, \quad \sum_{q=1}^p \Delta t_q \right] \quad (\text{S15})$$

In our optimization framework, we restrict the time step Δt_p to the positive range $\Delta t_p \in [\tau_{\min}/\Gamma_{\text{NL}}, \tau_{\max}/\Gamma_{\text{NL}}]$:

$$\Delta t_p \Gamma_{\text{NL}} = \tau_{\min} + (\tau_{\max} - \tau_{\min}) / (1 + e^{-X_p}), \quad (\text{S16})$$

where $\tau_{\min} > 0$ to avoid diverging physical rates in Eq. (S15). The parameter X_p is trainable and real. We parameterize δ_m^c , δ_m^e , and κ_m as

$$\delta_{m,p}^c/\Gamma_{\text{NL}} = \tau_{\min} D^c \arctan(d_{m,p}^c)/\pi \quad (\text{S17})$$

$$\kappa_{m,p}/\Gamma_{\text{NL}} = \tau_{\min} K \arctan(k_{m,p})/\pi + 1/2, \quad (\text{S18})$$

$$\delta_{m,p}^e/g = \tau_{\min} D^e \arctan(d_{m,p}^{(e)})/\pi \quad (\text{S19})$$

where $d_{m,p}^c$, $d_{m,p}^e$ and $k_{m,p}$ are *trainable* real parameters. $\delta_m^c(t_p) \in [-D_p^c/2, D_p^c/2]$, $\kappa_m(t_p) \in [0, K_p]$, and $\delta_m^e(t_p) \in [-D^e/2, D^e/2]$, which ensures that all physical rates are finite and the coupling is positive. Thus, D_c , K , and D^e determine the bounds of the control signals.

Finally, we parameterize \mathbf{C} , which is any real and symmetric matrix. To avoid the coupling of each cavity altering the cavity detuning, we set the diagonal of \mathbf{C} to zero. We then specify the elements of the upper triangle of \mathbf{C} using $M(M-1)/2$ real parameters that we train.

To initialize the trainable parameters, we specify an offset and a noise value. We draw each trainable parameter from a unit normal distribution. The drawn value is scaled by the noise parameter, and we add the offset.

B. Loss Function and Optimization

Using a gradient descent algorithm, we optimize our parameters with respect to the following cost function:

$$\mathcal{E}(\boldsymbol{\theta}) = \ln(\mathcal{I}) + \sum_{u \in \{\kappa, \delta^c, \delta^e\}} w_{\text{smooth}}^{(u)} \frac{1}{M} \sum_m \frac{\int_{-\infty}^{\infty} \left| \frac{du_m(t)}{dt} \right|^2 dt}{1 + \int_{-\infty}^{\infty} |u_m(t)|^2 dt} \quad (\text{S20})$$

The primary objective of the optimization is to achieve a small infidelity $\mathcal{I} < 0.001$, defined in the main text. However, we can optimize for the secondary objective of smooth signals using non-zero weight factors, $w_{\text{smooth}}^{(u)}$. The factors

$w_{\text{smooth}}^{(u)}$ for the three different types of control signals penalize fast variations of each type of control signal $u = \kappa, \delta^c$, or δ^e . The integrals are calculated numerically:

$$\int_{-\infty}^{\infty} \left| \frac{du(t)}{dt} \right|^2 dt = \sum_{p=1}^{N_{\text{bin}}+1} \frac{|u_p - u_{p-1}|^2}{0.5(\Delta t_p + \Delta \tau_{p-1})}, \quad \int_{-\infty}^{\infty} |u(t)|^2 dt = \sum_{p=1}^{N_{\text{bin}}} |u_p|^2 \Delta t_p, \quad (\text{S21})$$

where u_0 and $u_{N_{\text{bin}}+1}$ are not pieces of our time evolution but we include them in the integral of the derivative and set them to zero $u_0 = u_{N_{\text{bin}}+1} = 0$ in order to impose that our signal should go to zero at the start and end (we set $\Delta \tau_0 = \Delta \tau_1$ and $\Delta t_{N_{\text{bin}}+1} = \Delta \tau_{N_{\text{bin}}}$ when calculating the integral with the gradient). By regularizing the smoothness term, we limit the effective bandwidth:

$$B = \sqrt{\frac{\int_{-\infty}^{\infty} \left| \frac{du(t)}{dt} \right|^2 dt}{\int_{-\infty}^{\infty} |u(t)|^2 dt}}. \quad (\text{S22})$$

We note that the concept of a finite bandwidth only makes sense physically for continuous signals. For this reason, we use many time bins to approximate the continuous limit.

SIV. LOWER BOUND ON CZ-GATE DURATION

A. CZ Gate on Dual-Rail Qubits

We now prove the lower bound of the qubit-qubit CZ-gate duration when acting on dual-rail qubits for architectures that consist of linear optical devices and SPM elements, which evolve mode \hat{a}_m using Hamiltonian $-\hbar \chi_3 \hat{a}_m^\dagger \hat{a}_m \hat{a}_m^\dagger \hat{a}_m$. This evolution could be implemented using nonlinear cavities with dynamic coupling [S6]. With dual-rail encoding, the two-qubit logic states are:

$$|0,0\rangle_L = \hat{a}_1^\dagger \hat{a}_3^\dagger |0\rangle, \quad |0,1\rangle_L = \hat{a}_1^\dagger \hat{a}_4^\dagger |0\rangle, \quad |1,0\rangle_L = \hat{a}_2^\dagger \hat{a}_3^\dagger |0\rangle, \quad |1,1\rangle_L = \hat{a}_2^\dagger \hat{a}_4^\dagger |0\rangle, \quad (\text{S23})$$

where $|0\rangle$ is the vacuum state. Logical states are denoted by subscripts L , and, e.g., $|0,1\rangle_L$ is the state where the first qubit (encoded in modes 1 and 2) is in the logical 0 state (since the photon is in mode 1) while the second qubit (encoded in modes 3 and 4) is in the logical 1 (since the photon is in mode 4). The qubit-qubit CZ gate, represented by the operator \hat{U}_{CZ}^{bb} , should impart a sign-shift on the input if both qubits are in the logical 1 and do nothing otherwise. Thus, \hat{U}_{CZ}^{bb} written as a matrix in the basis of the four logical states is:

$$\hat{U}_{CZ}^{\text{bb}} = \begin{bmatrix} 1 & 0 & 0 & 0 \\ 0 & 1 & 0 & 0 \\ 0 & 0 & 1 & 0 \\ 0 & 0 & 0 & -1 \end{bmatrix}, \quad \text{basis} = \{|0,0\rangle_L, |0,1\rangle_L, |1,0\rangle_L, |1,1\rangle_L\}. \quad (\text{S24})$$

To impart this conditional π -phase shift, we need a nonlinear transformation of modes, as is immediately evident from the following. Consider a linear optical element that imparts a phase shift on each of our four modes $\mathbf{S}_{\text{phase}}$. In all considered gates, \hat{U}_{Gate} , we use the phase of $\langle 0,0 | \hat{U}_{\text{Gate}} | 0,0 \rangle_L$ as reference. Since $|0,0\rangle_L = \hat{a}_1^\dagger \hat{a}_3^\dagger |0\rangle$, we therefore let $\mathbf{S}_{\text{phase}}$ impart phase shifts only on \hat{a}_2 and \hat{a}_4 , with no loss of generality:

$$\mathbf{S}_{\text{phase}} = \begin{bmatrix} 1 & 0 & 0 & 0 \\ 0 & e^{-i\theta_2} & 0 & 0 \\ 0 & 0 & 1 & 0 \\ 0 & 0 & 0 & e^{-i\theta_4} \end{bmatrix}, \quad \text{basis} = \{\hat{a}_1, \hat{a}_2, \hat{a}_3, \hat{a}_4\}. \quad (\text{S25})$$

Note that $\mathbf{S}_{\text{phase}}$ applies a generalized single-qubit phase gate on the first qubit with phase shift $-\theta_2$, and a generalized single-qubit phase gate on the second qubit with phase shift $-\theta_4$. In the basis spanned by the logical states, the corresponding two-qubit gate \hat{U}_{phase} , which $\mathbf{S}_{\text{phase}}$ implements, is:

$$\hat{U}_{\text{phase}} = \begin{bmatrix} 1 & 0 & 0 & 0 \\ 0 & e^{-i\theta_4} & 0 & 0 \\ 0 & 0 & e^{-i\theta_2} & 0 \\ 0 & 0 & 0 & e^{-i(\theta_2+\theta_4)} \end{bmatrix}, \quad \text{basis} = \{|0,0\rangle_L, |0,1\rangle_L, |1,0\rangle_L, |1,1\rangle_L\}. \quad (\text{S26})$$

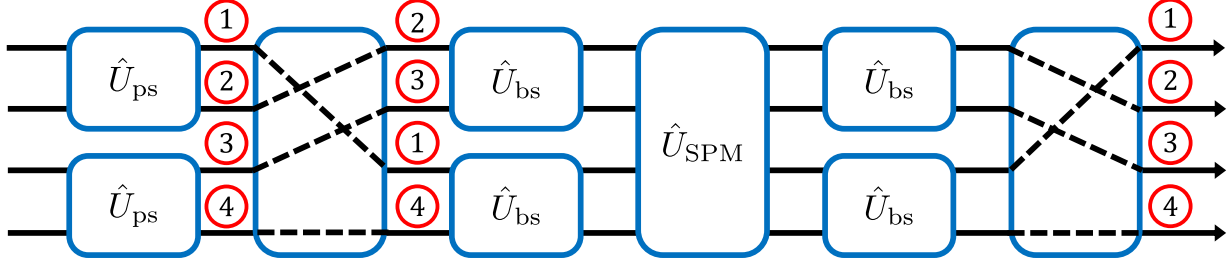


FIG. S2. Decomposition of the CZ gate into linear elements and an SPM element. We keep track of the original mode number using the numbers in red circles. $\hat{U}_{\text{ps}} = \exp\{i\hat{a}_\ell^\dagger \hat{a}_\ell \pi/2\}$ and $\hat{U}_{\text{bs}} = \exp\{i\hat{a}_\ell^\dagger \hat{a}_\ell \pi/2\} \exp\{-i(\hat{a}_u^\dagger \hat{a}_\ell + \hat{a}_\ell^\dagger \hat{a}_u)\pi/4\} \exp\{i\hat{a}_\ell^\dagger \hat{a}_\ell \pi/2\}$ are linear transformations, where we use u and ℓ to denote the upper (u) and lower (ℓ) port, respectively, when drawing the element. $\hat{U}_{\text{SPM}} = \exp\{i\chi_3 T \sum_{m=1}^4 \hat{a}_m^\dagger \hat{a}_m \hat{a}_m^\dagger \hat{a}_m\}$, where $T = \pi/(4\chi_3)$ is the SPM transformation.

From the above, it is clear that we cannot achieve a π -shift on $|1,1\rangle_L$ while imparting no phase shift on both $|0,1\rangle_L$ and $|1,0\rangle_L$. So we need a nonlinear element. In this case, we use SPM elements, which transform modes by $\exp(i\chi_3 T \sum_m \hat{a}_m^\dagger \hat{a}_m \hat{a}_m^\dagger \hat{a}_m)$ when the SPM is turned on for a duration T . Since we use dual-rail encoding, each two-qubit gate uses two photons. Thus, the rate of the nonlinear phase shift is $2\chi_3$ when two photons are in the same cavity and zero otherwise. This means that the time it takes to obtain a phase shift of ϕ is $T_\phi = \phi/(2\chi_3)$. To implement the CZ gate in minimal time, we neglect the duration of the linear operations, and therefore we want to construct the CZ gate using the smallest possible conditional phase shift. We therefore combine the linear gate \hat{U}_{phase} with the following gate \hat{U}_{cond} that applies a conditional phase shift to any of the logical basis states, except the reference state $|0,0\rangle_L$:

$$\hat{U}_{\text{cond}} = \begin{bmatrix} 1 & 0 & 0 & 0 \\ 0 & e^{i\phi_{01}} & 0 & 0 \\ 0 & 0 & e^{i\phi_{10}} & 0 \\ 0 & 0 & 0 & e^{i\phi_{11}} \end{bmatrix}, \quad \text{basis} = \{|0,0\rangle_L, |0,1\rangle_L, |1,0\rangle_L, |1,1\rangle_L\}, \quad (\text{S27})$$

where the conditional phase shifts $(\phi_{10}, \phi_{01}, \phi_{11})$ are positive since they are generated by $e^{i2\chi_3 t}$. The combination of \hat{U}_{phase} and \hat{U}_{cond} produces the following transformation:

$$\hat{U}_{\text{phase}} \hat{U}_{\text{cond}} = \begin{bmatrix} 1 & 0 & 0 & 0 \\ 0 & e^{i(\phi_{01}-\theta_4)} & 0 & 0 \\ 0 & 0 & e^{i(\phi_{10}-\theta_2)} & 0 \\ 0 & 0 & 0 & e^{i(\phi_{11}-(\theta_2+\theta_4))} \end{bmatrix}. \quad (\text{S28})$$

For the above to realize a CZ gate, we require $\theta_4 = \phi_{01}$, $\theta_2 = \phi_{10}$, and $\phi_{11} - (\theta_2 + \theta_4) = \pm\pi$. Inserting $\theta_4 = \phi_{01}$ and $\theta_2 = \phi_{10}$ into $\phi_{11} - (\theta_2 + \theta_4) = \pm\pi$, we obtain:

$$\phi_{11} - (\phi_{01} + \phi_{10}) = \pm\pi \quad (\text{S29})$$

We want to find the solution that minimizes the maximum of all conditional phase shifts: $\phi_{01}, \phi_{10}, \phi_{11}$. We separately consider the case where the right-hand side is $+\pi$ and $-\pi$, respectively. First, we consider $\phi_{11} - (\phi_{01} + \phi_{10}) = \pi$. In that case, $\phi_{11} = \pi + (\phi_{01} + \phi_{10})$, so $\phi_{11} > (\phi_{01} + \phi_{10})$, which means that ϕ_{11} is the largest of the three conditional phase shifts. The minimal ϕ_{11} is obtained for $\phi_{01} + \phi_{10} = 0$. We get $\phi_{11} = \pi$. This corresponds to the solution which does not utilize any linear phase shifts, which was already found in Ref. [S7]. We now consider the equation with $\phi_{11} - (\phi_{01} + \phi_{10}) = -\pi$, which implies that $\phi_{01} + \phi_{10} = \pi + \phi_{11}$. To minimize $\phi_{01} + \phi_{10}$, we minimize ϕ_{11} , which yields $\phi_{11} = 0$ and $\phi_{01} + \phi_{10} = \pi$. In order to minimize the maximum of ϕ_{01} and ϕ_{10} , we must choose $\phi_{01} = \phi_{10} = \pi/2$. Therefore, the minimal conditional phase shift is $\pi/2$. We conclude that the minimal duration of a qubit-qubit CZ gate with dual-rail encoding using linear elements and SPM elements is $T_{\min}^{CZ} = \pi/(4\chi_3)$.

In practice, we allow for a finite infidelity $\mathcal{I} > 0$, which permits smaller nonlinear phase shifts $\phi_{01} = \phi_{10} = \phi < \pi/2$ and thus shorter durations. By inserting $\theta_2 = \theta_4 = \pi/2$, $\phi_{11} = 0$, and $\phi_{01} = \phi_{10} = \phi$ into Eq. (S28) and defining $x = \pi/2 - \phi$, we obtain

$$\hat{U}_{CZ,x}^{\text{bb}} = \begin{bmatrix} 1 & 0 & 0 & 0 \\ 0 & e^{-ix} & 0 & 0 \\ 0 & 0 & e^{-ix} & 0 \\ 0 & 0 & 0 & -1 \end{bmatrix}, \quad \text{basis} = \{|0,0\rangle_L, |0,1\rangle_L, |1,0\rangle_L, |1,1\rangle_L\}. \quad (\text{S30})$$

We now calculate the infidelity using Eq. (9) in the main text. The target states of the CZ gate are:

$$\hat{U}_{\text{tar}} \left| \psi_{\text{in}}^{(1)} \right\rangle = |0,0\rangle_L, \quad \hat{U}_{\text{tar}} \left| \psi_{\text{in}}^{(2)} \right\rangle = |0,1\rangle_L, \quad \hat{U}_{\text{tar}} \left| \psi_{\text{in}}^{(3)} \right\rangle = |1,0\rangle_L, \quad \hat{U}_{\text{tar}} \left| \psi_{\text{in}}^{(4)} \right\rangle = -|1,1\rangle_L \quad (\text{S31})$$

The output states of the gate in Eq. (S30) are:

$$\hat{U}_{CZ,x}^{\text{bb}} \left| \psi_{\text{in}}^{(1)} \right\rangle = |0,0\rangle_L, \quad \hat{U}_{CZ,x}^{\text{bb}} \left| \psi_{\text{in}}^{(2)} \right\rangle = e^{-ix} |0,1\rangle_L, \quad \hat{U}_{CZ,x}^{\text{bb}} \left| \psi_{\text{in}}^{(3)} \right\rangle = e^{-ix} |1,0\rangle_L, \quad \hat{U}_{CZ,x}^{\text{bb}} \left| \psi_{\text{in}}^{(4)} \right\rangle = -|1,1\rangle_L. \quad (\text{S32})$$

The infidelity is thus:

$$\mathcal{I} = 1 - \frac{|1 + e^{-ix} + e^{-ix} + 1|^2}{16} = \sin^2(x/2). \quad (\text{S33})$$

We look for conditional phase shifts below $\pi/2$, so $x > 0$. By solving Eq. (S33) for x , we find:

$$x < 2 \sin^{-1}(\sqrt{\mathcal{I}}). \quad (\text{S34})$$

The lower bound on the conditional phase shift is then $\pi/2 - 2 \sin^{-1}(\sqrt{\mathcal{I}})$. The nonlinear phase shift as a function of time is $\phi = 2\chi_3 t$. Thus, the minimal gate duration is

$$T_{\text{min}}^{CZ}(\mathcal{I}) = \frac{\pi/4 - \sin^{-1}(\sqrt{\mathcal{I}})}{\chi_3}. \quad (\text{S35})$$

For $\mathcal{I} = 0.1\%$, the minimum duration is $0.754/\chi_3$. In the following, we find an analytical implementation with this duration using linear elements and SPM elements. The SPM element on each photonic mode could be realized with a dynamical SPM-nonlinear cavity that captures a photonic state, imparts the SPM phase shift while the cavity is closed, and releases the photonic state [S6]. We consider a device with four nonlinear cavities and four input-output channels, one per cavity. This device applies a unitary transformation $\hat{U}_{\text{SPM}} = \exp\left\{i\chi_3 T \sum_{m=1}^4 \hat{a}_m^\dagger \hat{a}_m^\dagger \hat{a}_m \hat{a}_m\right\}$, where $T = \pi/(4\chi_3)$ is the duration of time for which the photonic fields are evolved inside the closed cavities. Furthermore, we use the following linear devices with two input-output ports:

$$\mathbf{S}_{\text{ps}} = \begin{bmatrix} 1 & 0 \\ 0 & e^{-i\pi/2} \end{bmatrix}, \quad \mathbf{S}_{\text{bs}} = \frac{1}{\sqrt{2}} \begin{bmatrix} 1 & 1 \\ 1 & -1 \end{bmatrix}, \quad \text{basis} = \{\hat{a}_u, \hat{a}_\ell\}, \quad (\text{S36})$$

where we call the two modes of the input ports u and ℓ to denote the upper (u) and lower (ℓ) port when drawing the device in Fig. S2. The corresponding unitary operators are $\hat{U}_{\text{ps}} = \exp\left\{i\hat{a}_\ell^\dagger \hat{a}_\ell \pi/2\right\}$ and $\hat{U}_{\text{bs}} = \exp\left\{i\hat{a}_\ell^\dagger \hat{a}_\ell \pi/2\right\} \exp\left\{-i(\hat{a}_u^\dagger \hat{a}_\ell + \hat{a}_\ell^\dagger \hat{a}_u)\pi/4\right\} \exp\left\{i\hat{a}_\ell^\dagger \hat{a}_\ell \pi/2\right\}$. In Fig. S2, we show how to combine these elements to implement a CZ gate with duration $T = \pi/(4\chi_3)$ ($T = 0.754/\chi_3$ for $\mathcal{I} = 0.1\%$). Phase shifts, \mathbf{S}_{ps} , are applied to modes 1 and 2 and modes 3 and 4, respectively, to implement \hat{U}_{phase} . We use \mathbf{S}_{bs} to implement the conditional gate \hat{U}_{cond} , where a phase shift of $\pi/2$ is applied if the input is $|1,0\rangle_L$ or $|0,1\rangle_L$, i.e., if there is a photon in either both mode 2 and 3 or both mode 1 and 4. The idea here is to couple each pair of modes (mode 1 and 4 and mode 2 and 3, respectively) using \mathbf{S}_{bs} , which transforms, e.g., $|1_1, 1_4\rangle$ into $(|2_1, 0_4\rangle - |0_1, 2_4\rangle)/\sqrt{2}$. Thus, for input $|1,0\rangle_L$ or $|0,1\rangle_L$ only, the beam splitter transformations produce a superposition of states where the two photons are in the same mode. We cascade this output into \hat{U}_{SPM} , which imparts a $\pi/2$ -phase shift only if two photons are in the same mode, i.e., if the original state was $|1,0\rangle_L$ or $|0,1\rangle_L$. We then transform the state back to the code space by using \mathbf{S}_{bs} on each pair of modes. If we allow an infidelity $\mathcal{I} = 0.1\%$, then we only need to spend time $T = 0.754/\chi_3$ inside the cavities.

Using the RQPN, we find an implementation with duration $0.773/\chi_3$ using numerical optimization. We document the rates of coupling and detuning in Fig. S3(a) and (b), the coupling matrix in Fig. S3(c), and the evolution of logical inputs in time in Fig. S3(d).

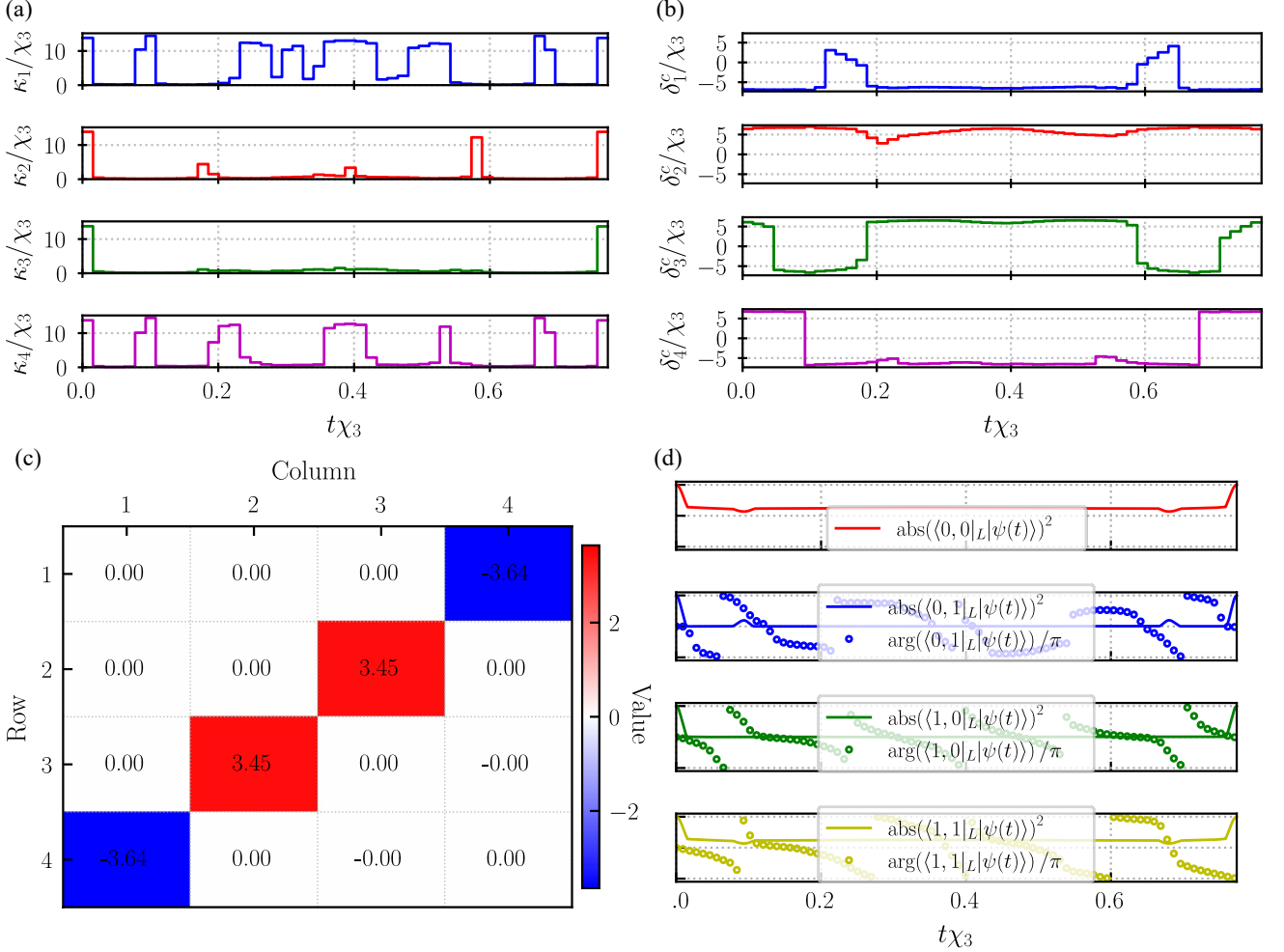


FIG. S3. Cavity coupling (a), detuning (b), coupling matrix (c), and time evolution of the RQPN state $|\psi(t)\rangle$ for each logical input (d) for the qubit-qubit CZ gate with dual-rail encoding, implemented using an RQPN with SPM interactions. In (d), the phase, $\arg(\cdot)$, in each subplot is calculated relative to the phase of $\langle 0,0|_L|\psi(t)\rangle$ for input $|0,0\rangle_L$. Specifications for the optimization were: Control signals with $N_{\text{bin}} = 50$ time bins, maximum detuning amplitude $D^c/2 = 7.5/\chi_3$ and maximum coupling $K = 15/\chi_3$. The minimum and maximum time duration were set to $N_{\text{bin}}\tau_{\min} = 0.725/\chi_3$ and $N_{\text{bin}}\tau_{\max} = 0.775/\chi_3$. The trained detuning and coupling parameters $d_{m,p}^c$ and $k_{m,p}$ were initialized with an offset of 0 and noise of 0.1. The trained time step parameters X_p were initialized with an offset of 0 and a noise of 0.1. The trained off-diagonal coupling matrix elements were initialized with an offset of 0 and a noise of 1.0. The cost function did not include smoothing terms $w_{\text{smooth}}^{(\delta^c)} = 0$ and $w_{\text{smooth}}^{(\kappa)} = 0$. We used the **Adam** optimizer with learning rate 0.01 for 11144 epochs to reach $\mathcal{I} < 0.1\%$.

B. CZ Gate using a Qutrit and a Qubit

In this section, we prove that the lower bound for the duration of the qubit-qubit CZ gate is also a lower bound on the duration of the qubit-qutrit CZ gate, defined in Eq. (10) in the main text. In this case, there is an additional mode, $m = 5$, and one of the photons encodes a qutrit rather than a qubit:

$$|0,0\rangle_L = \hat{a}_1^\dagger \hat{a}_3^\dagger |0\rangle, \quad |0,1\rangle_L = \hat{a}_1^\dagger \hat{a}_4^\dagger |0\rangle, \quad |1,0\rangle_L = \hat{a}_2^\dagger \hat{a}_3^\dagger |0\rangle, \quad |1,1\rangle_L = \hat{a}_2^\dagger \hat{a}_4^\dagger |0\rangle, \\ |0,2\rangle_L = \hat{a}_1^\dagger \hat{a}_5^\dagger |0\rangle, \quad |1,2\rangle_L = \hat{a}_2^\dagger \hat{a}_5^\dagger |0\rangle.$$

The linear and conditional gate can thus be written as:

$$\hat{U}_{\text{phase}} = \begin{bmatrix} 1 & 0 & 0 & 0 & 0 & 0 \\ 0 & e^{-i\theta_4} & 0 & 0 & 0 & 0 \\ 0 & 0 & e^{-i\theta_2} & 0 & 0 & 0 \\ 0 & 0 & 0 & e^{-i(\theta_2+\theta_4)} & 0 & 0 \\ 0 & 0 & 0 & 0 & e^{-i\theta_5} & 0 \\ 0 & 0 & 0 & 0 & 0 & e^{-i(\theta_2+\theta_5)} \end{bmatrix}, \quad \text{basis} = \{|0,0\rangle_L, |0,1\rangle_L, |1,0\rangle_L, |1,1\rangle_L, |0,2\rangle_L, |1,2\rangle_L\}. \quad (\text{S37})$$

$$\hat{U}_{\text{cond}} = \begin{bmatrix} 1 & 0 & 0 & 0 & 0 & 0 \\ 0 & e^{i\phi_{01}} & 0 & 0 & 0 & 0 \\ 0 & 0 & e^{i\phi_{10}} & 0 & 0 & 0 \\ 0 & 0 & 0 & e^{i\phi_{11}} & 0 & 0 \\ 0 & 0 & 0 & 0 & e^{i\phi_{02}} & 0 \\ 0 & 0 & 0 & 0 & 0 & e^{i\phi_{12}} \end{bmatrix}, \quad \text{basis} = \{|0,0\rangle_L, |0,1\rangle_L, |1,0\rangle_L, |1,1\rangle_L, |0,2\rangle_L, |1,2\rangle_L\}. \quad (\text{S38})$$

From the qubit-qubit CZ gate, we know that $\theta_2 = \theta_4 = \phi_{10} = \phi_{01} = \pi/2$, which already requires a conditional phase shift of at least $\pi/2$. For $\theta_5 = \phi_{02} = 0$ and $\phi_{12} = \theta_2 = \pi/2$, $\hat{U}_{\text{phase}}\hat{U}_{\text{cond}}$ would give the required CZ gate transformation. We conclude that $\pi/2$ is also a lower bound on the phase shift required to implement a qubit-qutrit CZ gate. The best-case infidelity as a function of the difference x between the conditional phase needed and $\pi/2$, is the same as it is for the qubit-qubit CZ gate:

$$\mathcal{I} = 1 - \frac{|3 + 3e^{-ix}|^2}{6^2} = 1 - (9/36)4 \cos^2 x/2 = \sin^2(x/2), \quad (\text{S39})$$

which corresponds to the same lower bound on the duration of $T = 0.754/\chi_3$ for $\mathcal{I} = 0.1\%$.

Unlike the qubit-qubit CZ gate, we have not discovered a physical implementation of the qubit-qutrit CZ gate that meets this lower bound, and there is no guarantee that an implementation with $T = \pi/(4\chi_3)$ exists. Using the RQPN, we find an implementation with a duration of $0.89/\chi_3$ for $\mathcal{I} = 0.1\%$ using numerical optimization. We document the rates of coupling and detuning in Fig. S4(a) and (b), the coupling matrix in Fig. S4(c), and the evolution of logical inputs in time in Fig. S4(d).

C. Numerical Optimization of CZ Gate with TLE Interactions

For comparison, we have also considered the qubit-qubit CZ gate implemented using TLEs. Using the RQPN, our optimized implementation has a duration of $3.98/g$ for $\mathcal{I} = 0.1\%$. This is comparable to the results in Ref. [S7]. We document the cavity-waveguide coupling, detuning of cavities, and detuning of TLEs in Fig. S5(a), (b), and (c), the coupling matrix in Fig. S5(d), and the evolution of logical inputs in time in Fig. S5(e).

SV. ADDITIONAL PLOTS OF THE RESULTS FOR A THREE-QUBIT TOFFOLI GATE

Using the RQPN, we find an implementation of the three-qubit Toffoli gate. For the optimization configuration that yielded the shortest duration, we used a fixed duration of $2.00/\chi_3$ for $\mathcal{I} < 0.3\%$. We plot the cavity-waveguide coupling and detuning in Fig. S6(a) and (b), the coupling matrix in Fig. S6(c), and the time evolution of each logical state in Fig. S6(d).

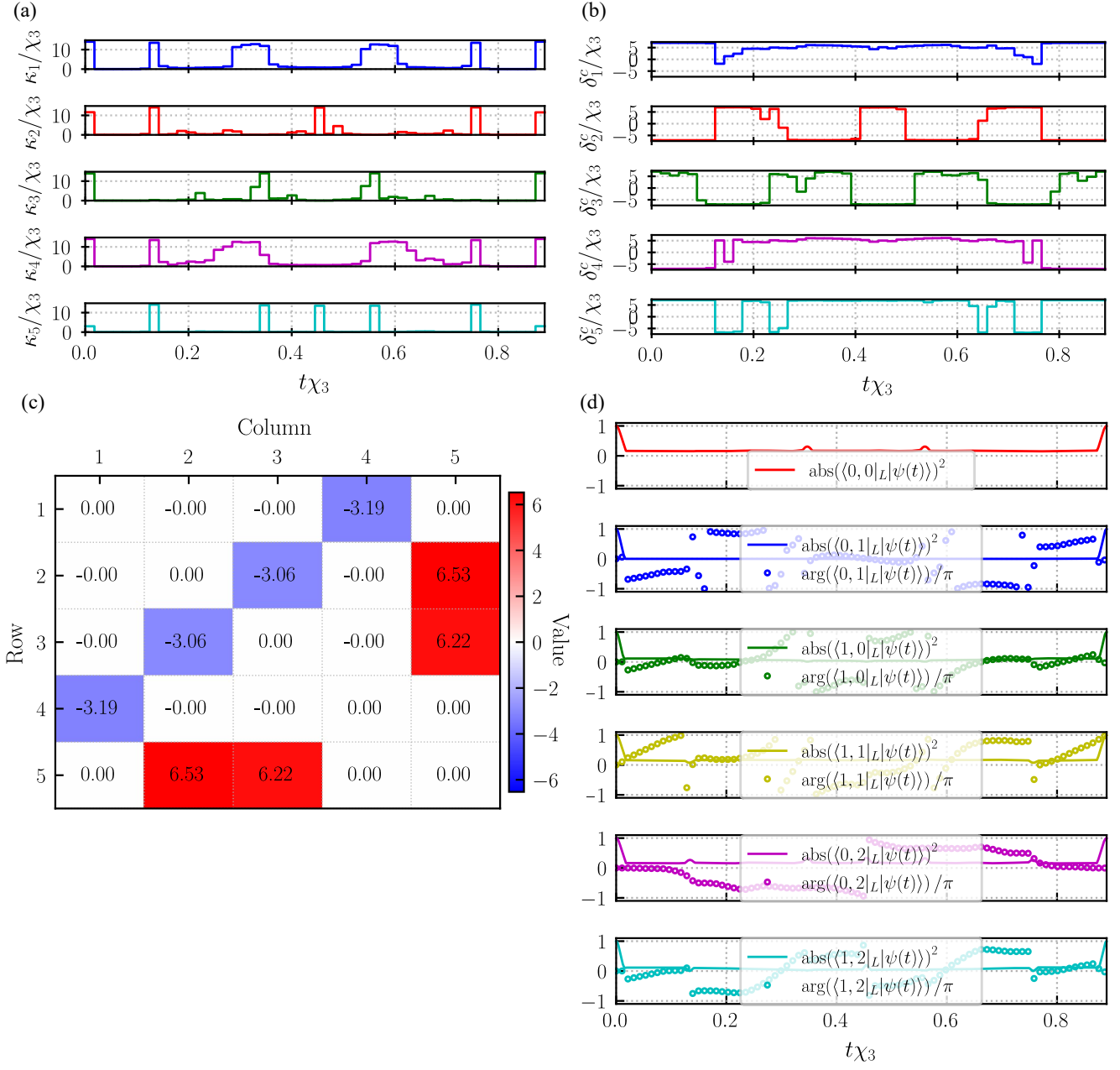


FIG. S4. Cavity coupling (a), detuning (b), coupling matrix (c), and time evolution of the RQPN state $|\psi(t)\rangle$ for each logical input (d) for the qubit-qutrit *CZ* gate with dual-rail encoding, implemented using an RQPN with SPM interactions. In (d), the phase, $\arg(\cdot)$, in each subplot is calculated relative to the phase of $\langle 0,0|_L |\psi(t)\rangle$ for input $|0,0\rangle_L$. Specifications for the optimization were: Control signals with $N_{\text{bin}} = 50$ time bins, maximum detuning amplitude $D^c/2 = 7.5/\chi_3$ and maximum coupling $K = 15/\chi_3$. The minimum and maximum time duration were set to $N_{\text{bin}}\tau_{\text{min}} = 0.84/\chi_3$ and $N_{\text{bin}}\tau_{\text{max}} = 0.89/\chi_3$. The trained detuning and coupling parameters $d_{m,p}^c$ and $k_{m,p}$ were initialized with an offset 0 and a noise of 0.1. The trained timestep parameters X_p were initialized with an offset of 0 and a noise level of 0.1. The trained off-diagonal coupling matrix elements were initialized with an offset of 0 and a noise of 1.0. The cost function did not include smoothing terms $w_{\text{smooth}}^{(\delta^c)} = w_{\text{smooth}}^{(\kappa)} = 0$. We used the **Adam** optimizer with learning rate 0.01 for 29079 epochs to reach $\mathcal{I} < 0.1\%$.

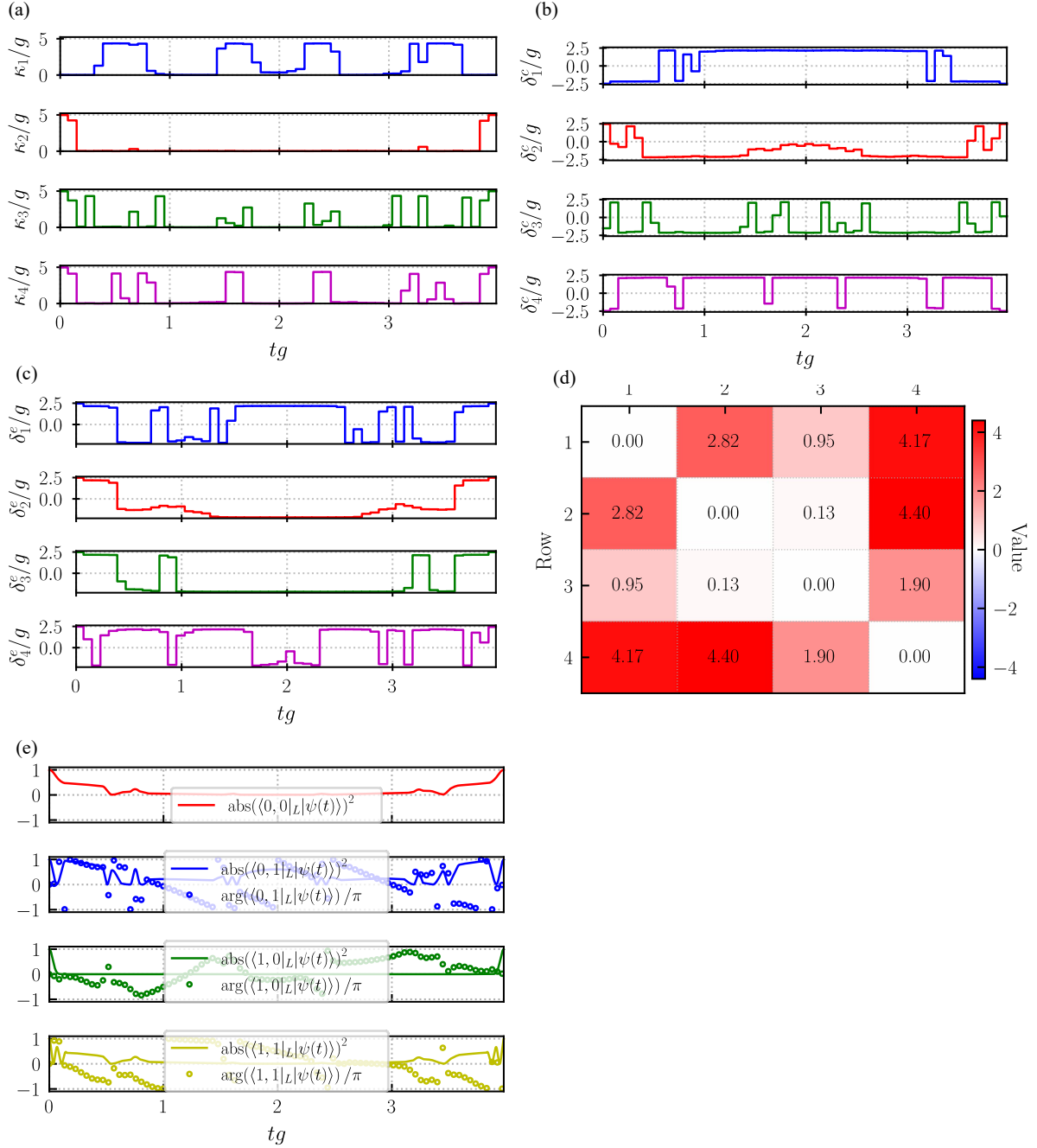


FIG. S5. Cavity coupling (a), cavity detuning (b), TLE detuning (c), coupling matrix (d), and time evolution of the RQPN state $|\psi(t)\rangle$ for each logical input (e) for the qubit-qubit CZ gate with dual-rail encoding, implemented using an RQPN with TLE interactions. In (e), the phase, $\arg(\cdot)$, in each subplot is calculated relative to the phase of $\langle 0,0|_L|\psi(t)\rangle$ for input $|0,0\rangle_L$. Specifications for the optimization were: Control signals with $N_{\text{bin}} = 50$ time bins, maximum detuning amplitudes, $D^c/2 = 2.5/g$ and $D^e/2 = 2.5/g$, and maximum coupling $K = 5/g$. The minimum and maximum time duration were set to $N_{\text{bin}}\tau_{\text{min}} = 3.5/g$ and $N_{\text{bin}}\tau_{\text{max}} = 4.0/g$. The trained detunings and coupling parameters $d_{m,p}^c$, $d_{m,p}^e$, and $k_{m,p}$ were initialized with an offset of 0 and a noise of 0.01. The trained time-step parameters X_p were initialized with an offset of 0 and a noise of 0.01. The trained off-diagonal coupling matrix elements were initialized with an offset of 1.0 and a noise of 0.1. The cost function did not include smoothing terms $w_{\text{smooth}}^{(\delta^c)} = w_{\text{smooth}}^{(\delta^e)} = w_{\text{smooth}}^{(\kappa)} = 0$. We used the **Adam** optimizer with learning rate 0.01 for 23391 epochs to reach $\mathcal{I} < 0.1\%$.

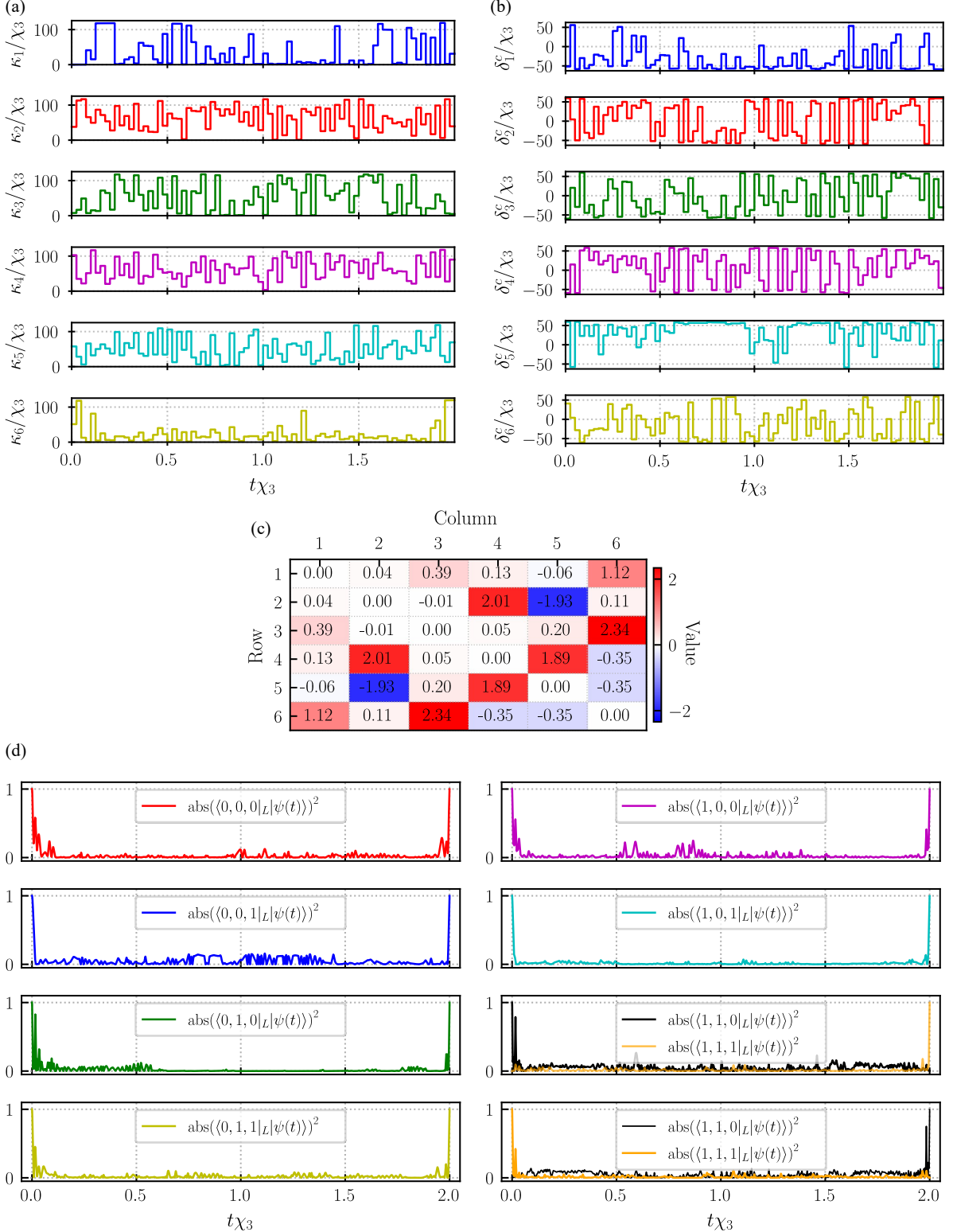


FIG. S6. Cavity coupling (a), cavity detuning (b), coupling matrix (c), and time evolution of the RQPN state $|\psi(t)\rangle$ for each logical input (d) for the three-qubit Toffoli gate with dual-rail encoding, implemented using an RQPN with SPM interactions. In (d), the phases of the inner products have been omitted to make the plots more readable. Specifications for the optimization were: Control signals with $N_{\text{bin}} = 80$ time bins, maximum detuning amplitude $D^c/2 = 75/\chi_3$ and maximum coupling $K = 150/\chi_3$. The minimum and maximum time duration were set to $N_{\text{bin}}\tau_{\text{min}} = 1.6/\chi_3$ and $N_{\text{bin}}\tau_{\text{max}} = 2.4/\chi_3$. The trained detuning parameters $d_{m,p}^c$ were initialized with an offset of 0 and a noise of 0. The trained coupling parameters $\kappa_{m,p}^c$ were initialized with an offset of 0 and a noise of 0.1. The time-step parameters X_p were fixed at 0, such that the time duration is $T = 2.0/\chi_3$. The trained off-diagonal coupling matrix elements were initialized with an offset of 0 and a noise of 1.0. The cost function did not include smoothing terms, $w_{\text{smooth}}^{(\delta^c)} = 0$ and $w_{\text{smooth}}^{(\kappa)} = 0$. We used the **Adam** optimizer with learning rate 0.012 for 28273 epochs to reach $\mathcal{I} < 0.3\%$.

SVI. ADDITIONAL PLOTS OF THE RESULTS FOR A ONE-WAY QUANTUM REPEATER

Using the RQPN, we find implementations of the measurement-free one-way quantum repeater. Using SPM nonlinearities, we split the repeater into two steps. For the step that corrects for photon loss in mode 1, we document the rates of coupling and detuning in Fig. S7(a) and (b) and the evolution of each input state in time in Fig. S7(c). For the step that corrects for photon loss in mode 2, we document the rates of coupling and detuning in Fig. S8(a) and (b) and the evolution of input states in time in Fig. S8(c). Using TLEs, we implement the full repeater using the rates of coupling and detuning of cavities and TLEs in Fig. S9(a-c) with corresponding time evolution of the RQPN state for each orthogonal input state in S9(d).

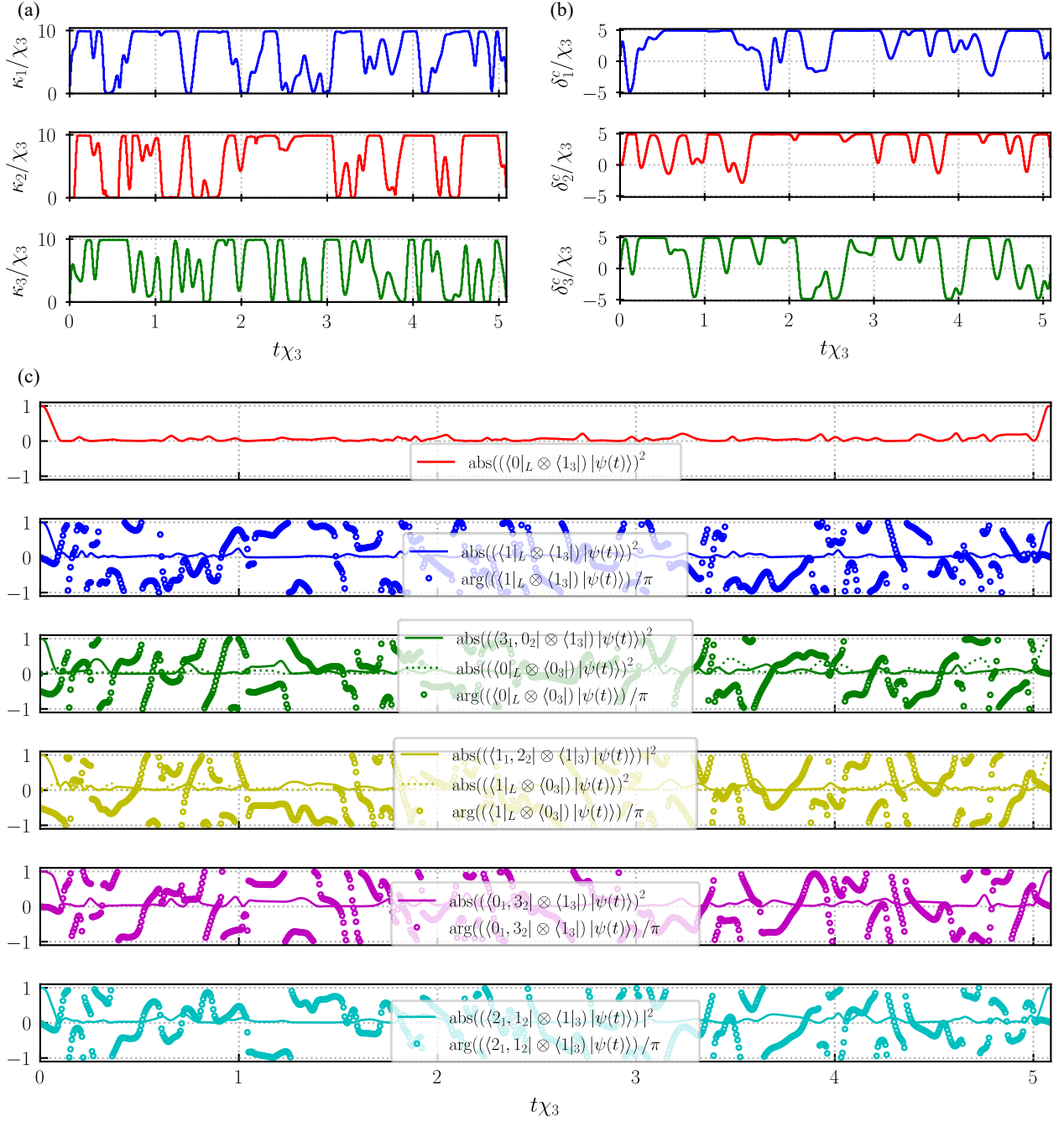


FIG. S7. Cavity coupling (a), cavity detuning (b), and time evolution of the RQPN state $|\psi(t)\rangle$ for all six orthogonal input states (c) for step one of the measurement-free repeater (correcting photon loss in mode 1), implemented using an RQPN with SPM interactions. In (c), the phase, $\arg(\cdot)$, in each subplot is calculated relative to the phase of $(|0\rangle_L \otimes |1_3\rangle) |\psi(t)\rangle$ for input $|0\rangle_L \otimes |1_3\rangle$ to confirm that there is no phase difference at output between any inputs. Specifications for the optimization were: Control signals with $N_{\text{bin}} = 640$ time bins, maximum detuning amplitude $D^c/2 = 5/\chi_3$ and maximum coupling $K = 10/\chi_3$. The minimum and maximum time duration were set to $N_{\text{bin}}\tau_{\text{min}} = 5.06/\chi_3$ and $N_{\text{bin}}\tau_{\text{max}} = 5.12/\chi_3$. The trained detuning parameters $d_{m,p}^c$ were initialized with an offset of 1 and a noise of 0.01. The trained coupling parameters $k_{m,p}^c$ were initialized with an offset of 0 and a noise of 0.01. The time-step parameters X_p were fixed at 0, such that the time duration is fixed at $5.09/\chi_3$. The off-diagonal coupling matrix elements were fixed at 1 and the diagonal elements at 0. The cost function included bandwidth penalty terms with $w_{\text{smooth}}^{(\delta^c)} = 0.006$ and $w_{\text{smooth}}^{(\kappa)} = 0.015$. We used the **Adam** optimizer with learning rate 0.01 for 17894 epochs to reach $\mathcal{I} < 0.05\%$.

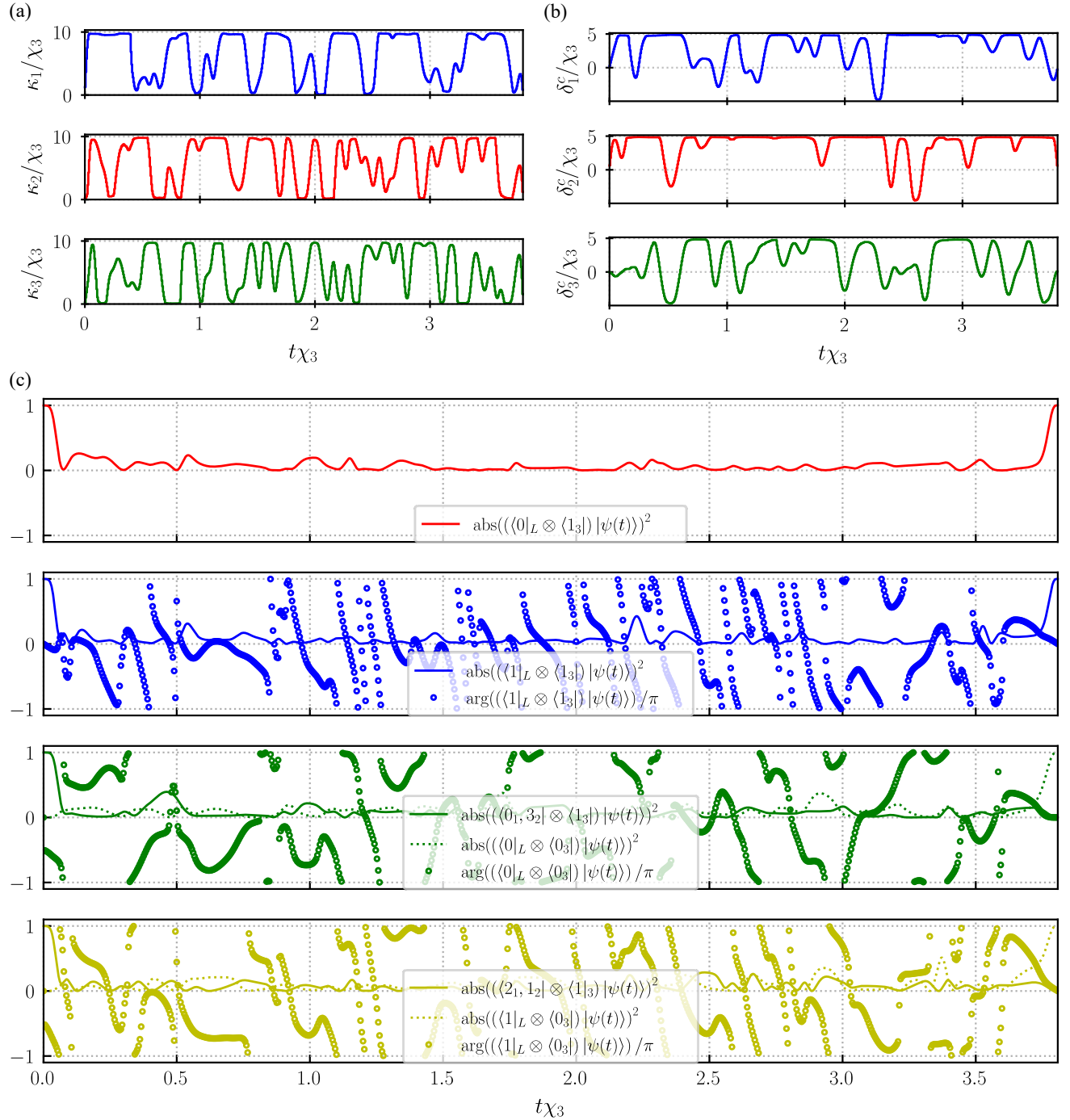


FIG. S8. Cavity coupling (a), cavity detuning (b), and time evolution of the RQPN state $|\psi(t)\rangle$ for all four orthogonal input states (c) for step two of the measurement-free repeater (correcting photon loss in mode 2), implemented using an RQPN with SPM interactions. In (c), the phase, $\text{arg}(\cdot)$, in each subplot is calculated relative to the phase of $(\langle 0|_L \otimes \langle 1_3 |) |\psi(t)\rangle$ for input $|0\rangle_L \otimes |1_3\rangle$ to confirm that there is no phase difference at output between any inputs. Specifications for the optimization were: Control signals with $N_{\text{bin}} = 640$ time bins, maximum detuning amplitude $D^c/2 = 5/\chi_3$ and maximum coupling $K = 10/\chi_3$. The minimum and maximum time duration were set to $N_{\text{bin}}\tau_{\text{min}} = 3.78/\chi_3$ and $N_{\text{bin}}\tau_{\text{max}} = 3.84/\chi_3$. The trained detuning parameters $d_{m,p}^c$ were initialized with an offset of 1 and a noise of 0.01. The trained coupling parameters $k_{m,p}^c$ were initialized with an offset of 0 and a noise of 0.01. The time-step parameters X_p were fixed at 0, such that the time duration is $T = 3.81/\chi_3$. The off-diagonal coupling matrix elements were fixed at 1 and the diagonal elements at 0. The cost function included bandwidth penalty terms with $w_{\text{smooth}}^{(\delta^c)} = 0.0035$ and $w_{\text{smooth}}^{(\kappa)} = 0.01$. We used the **Adam** optimizer with learning rate 0.01 for 11876 epochs to reach $\mathcal{I} < 0.05\%$.

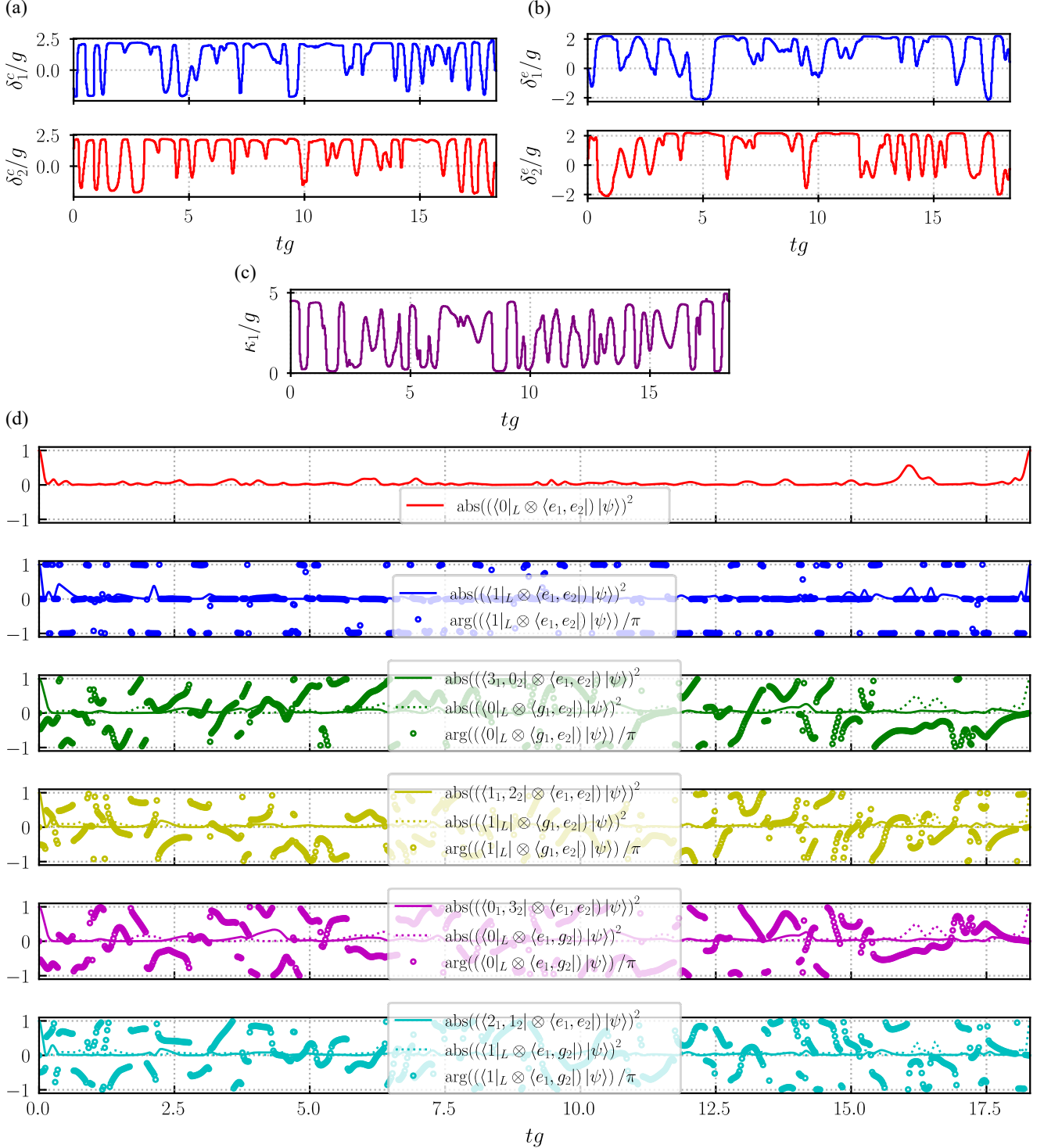


FIG. S9. Cavity detuning (a), TLE detuning (b), cavity coupling for both cavities (c), and time evolution of the RQPN state $|\psi(t)\rangle$ for all six orthogonal input states (d) for the measurement-free repeater, implemented using an RQPN with TLEs. In (d), the phase $\text{arg}(\cdot)$ in each subplot is calculated relative to the phase of $(\langle 0|_L \otimes \langle e_1, e_2 | \rangle |\psi(t)\rangle)$ for input $|0\rangle_L \otimes |e_1, e_2\rangle$ to confirm that there is no phase difference at output between any inputs. Specifications for the optimization were: Control signals with $N_{\text{bin}} = 640$ time bins, maximum detuning amplitude $D^c/2 = 2.5/g$, and maximum coupling $K = 5/g$. The minimum and maximum time duration were set to $N_{\text{bin}}\tau_{\text{min}} = 16.72/g$ and $N_{\text{bin}}\tau_{\text{max}} = 18.32/g$. The trained detuning parameters $d_{m,p}^c$ and $d_{m,p}^e$ were initialized with an offset of 1 and noise of 0.01. The trained coupling parameters $k_{m,p}^c$ were initialized with an offset of 0 and a noise of 0.01. The trained time-step parameters X_p were initialized with an offset of 0 and a noise of 0.01. The off-diagonal coupling matrix elements were fixed at 1 and the diagonal elements at 0. The cost function included bandwidth penalty terms with $w_{\text{smooth}}^{(\delta^c)} = 0.005$, $w_{\text{smooth}}^{(\delta^e)} = 0.005$, and $w_{\text{smooth}}^{(\kappa)} = 0.002$. We used the Adam optimizer with learning rate 0.01 for 8951 epochs to reach $\mathcal{I} < 0.1\%$.

- [S1] J. Gough and M. R. James, [IEEE Transactions on Automatic Control](#) **54**, 2530 (2009).
- [S2] J. Gough and M. R. James, [Communications in Mathematical Physics](#) **287**, 1109 (2009).
- [S3] J. Combes, J. Kerckhoff, and M. Sarovar, [Advances in Physics: X](#) **2**, 784 (2017).
- [S4] M. Houde, W. McCutcheon, and N. Quesada, [Canadian Journal of Physics](#) **102**, 497 (2024).
- [S5] S. Krastanov, M. Heuck, J. H. Shapiro, P. Narang, D. R. Englund, and K. Jacobs, [Nature Communications](#) **12**, 191 (2021).
- [S6] M. Heuck, K. Jacobs, and D. R. Englund, [Phys. Rev. Lett.](#) **124**, 160501 (2020).
- [S7] S. Krastanov, K. Jacobs, G. Gilbert, D. R. Englund, and M. Heuck, [npj Quantum Information](#) **8**, 103 (2022).